eprints@whiterose.ac.uk
https://eprints.whiterose.ac.uk/

RESEARCH ARTICLE

WILEY

Adaptive hierarchical refinement of NURBS in cohesive fracture analysis

Lin Chen[1] | Erik Jan Lingen[2] | René de Borst[1]

[1]Department of Civil and Structural Engineering, University of Sheffield, Sheffield, S1 3JD, UK

[2]Dynaflow Research Group, Zoetermeer, 2719 EB, Netherlands

Correspondence
René de Borst, Department of Civil and Structural Engineering, University of Sheffield, Sheffield S1 3JD, UK.
Email: r.deborst@sheffield.ac.uk

Summary

Adaptive hierarchical refinement in isogeometric analysis is developed to model cohesive crack propagation along a prescribed interface. In the analysis, the crack is introduced by knot insertion in the NURBS basis, which yields C^{-1} continuous basis functions. To capture the stress state smoothly ahead of the crack tip, the hierarchical refinement of the spline basis functions is used starting from a coarse initial mesh. A multilevel mesh is constructed, with a fine mesh used for quantifying the stresses ahead of the crack tip, knot insertion to insert the crack, and coarsening in the wake of the crack tip, since a lower resolution suffices there. This technique can be interpreted as a moving mesh around the crack tip. To ensure compatibility with existing finite element programs, an element-wise point of view is adopted using Bézier extraction. A detailed description is given how the approach can be implemented in a finite element data structure. The accuracy of the approach to cohesive fracture modelling is demonstrated by several numerical examples, including a double cantilever beam, an L-shaped specimen, and a fibre embedded in an epoxy matrix.

KEYWORDS

cohesive zone model, fracture, hierarchical refinement, isogeometric analysis, NURBS

1 | INTRODUCTION

The numerical simulation of fracture is a technically relevant and scientifically challenging issue and has been a focal point of attention since the early simulations in the 1960s[1,2] see also de Borst and de Borst et al[3,4] for overviews. From the very beginning, two different approaches have been pursued, discrete methods in which cracks are treated as geometric discontinuities, leading to topological changes,[1] and the distributed, or smeared approach, in which discontinuity is *modelled* by distributing it over a small, but finite band (with concomitant high local strains), eg, Rashid.[2] Later, the smeared approaches were cast in a damage format, eg, de Borst and Gutiérrez,[5] and more recently, phase-field models were introduced to describe brittle fracture in an elegant manner.[6-9] The close relation between phase-field models for brittle fracture and gradient-enhanced continuum damage models was recently discussed in detail, including similarities and differences.[10]

In spite of the conceptual elegance and its ability to represent complex crack patterns in a straightforward manner,[11,12] the phase-field approach to brittle fracture cannot be extended easily to cohesive fracture. A framework has been published,[13] but subsequent investigations[14,15] have put question marks on how a phase-field approach for cohesive fracture can be developed on unstructured meshes. This has motivated the further development of discrete approaches for cohesive fracture, which is

applicable to fracture processes in many quasibrittle and ductile materials, in particular when the size of the fracture process zone is nonnegligible compared to the structural dimensions.

Following the early work in Ngo and Scordelis,[1] in which fracture was simply modelled by the release of double nodes at existing element boundaries, much research has been undertaken to let the crack path evolve independent from the original discretisation. Mesh refinement,[16-19] and the introduction of the extended finite element method[20-22] are notable developments. With respect to the latter, it is noted that a straightforward extension to cohesive fracture has been achieved.[23-25]

More recently, the flexibility of isogeometric analysis, which uses B-splines instead of the traditional Lagrange polynomials as basis functions, has been exploited to lower the order of continuity to C^{-1}, thus locally creating a discontinuity.[26] Applicable to any fracture model, in principle, the approach has been utilised in several cases of adhesive fracture—using Non-Uniform Rational B-Splines (NURBS)—and cohesive fracture—using T-splines.[26] Alternatives to this approach of discrete crack modelling within the framework of isogeometric analysis are isogeometric interface elements,[27-29] which is particularly useful when the crack propagation path is known, Powell-Sabin B-splines, which can exploit standard remeshing algorithms for triangles,[30] and an approach that is rooted in computational contact mechanics.[31]

Even though the higher-order continuity of the basis functions in isogeometric analysis provides a much improved stress prediction, this continuity can be reduced near a crack tip. Hence, it is desirable to locally refine the discretisation. Adaptive hierarchical refinement is a powerful tool to achieve this within the framework of isogeometric analysis, and herein, we will describe how this can be done using Truncated Hierarchical NURBS. Moreover, we will show how Truncated Hierarchical NURBS can be coarsened, eg, in the wake of a crack tip where a less dense mesh suffices. In this paper, an element point of view is adopted, whereby Bézier extraction is exploited to cast isogeometric analysis in a framework, which uses standard finite element datastructures,[32,33] which is an improvement on earlier work using the concept of knot insertion to simulate cracking.[26]

To provide a proper background, we will first provide a succinct description of cohesive fracture modelling, followed by a recapitulation how fracture can be embedded within the isogeometric concept using continuity reduction. Next, fundamentals of hierarchical basis functions and refinement are summarised, and the use of hierarchical refinement in the analysis of cracking is discussed. An important issue is the implementation of hierarchical refinement. This is treated in some detail, including algorithmic aspects and data structures. Finally, some numerical examples are presented to validate the approach and conclusions are drawn.

2 | COHESIVE ZONE FORMULATION

Introduced in Dugdale and Barenblatt,[34,35] cohesive zone models are now widely used to model fracture, especially in quasibrittle and ductile materials.[36,37] Cohesive zone models essentially relate the tractions on a two-dimensional surface in a three-dimensional body to the crack opening and the crack sliding. The very fact that this so-called traction-separation law acts on a surface, which is of a lower dimension than the surrounding three-dimensional continuum, entails some complications.[38,39] However, when the crack path is known a priori as, for instance, in delamination of composite structures, interface elements can be embedded in the continuum at predefined locations, thus leading to a relatively straightforward discretisation.[40-45]

In a cohesive zone model, a crack is represented as an interface Γ_c in the physical domain Ω, Figure 1. In this contribution, the interface Γ_c is assumed to be predefined, as is the case of crack propagation along a material interface. Small displacement gradients have been assumed, so that the kinematic equations read

$$\boldsymbol{\varepsilon} = \frac{1}{2}\left(\nabla\mathbf{u} + (\nabla\mathbf{u})^{\mathrm{T}}\right) \qquad \text{on} \qquad \Omega; \qquad [\![\mathbf{u}]\!] = \mathbf{u}^+ - \mathbf{u}^- \qquad \text{on} \qquad \Gamma_c, \tag{1}$$

where $\boldsymbol{\varepsilon}$ is the infinitesimal strain tensor.

The crack opening $[\![\mathbf{u}]\!]$ is defined in the global coordinate system (x_1, x_2), where it is noted that the extension to three dimensions is straightforward. The crack sliding and the crack opening in the local coordinate system (s, n) (Figure 1) are given by

$$[\![\boldsymbol{v}]\!] = ([\![v_s]\!], \quad [\![v_n]\!])^{\mathrm{T}} = \mathbf{R}[\![\mathbf{u}]\!] = \mathbf{R}\left([\![u_{x_1}]\!], \quad [\![u_{x_2}]\!]\right)^{\mathrm{T}} \tag{2}$$

with $\mathbf{R}$ as the rotation matrix.[27]

Assuming linear elastic material behaviour, the equilibrium equations in their strong form read

$$\begin{cases} \nabla \cdot \boldsymbol{\sigma} = \mathbf{0} & \text{on} \quad \Omega \\ \mathbf{u} = \hat{\mathbf{u}} & \text{on} \quad \Gamma_u \\ \boldsymbol{\sigma} \cdot \mathbf{n} = \hat{\mathbf{t}} & \text{on} \quad \Gamma_t \\ \boldsymbol{\sigma} \cdot \mathbf{n} = \mathbf{t}([\![\mathbf{u}]\!]) & \text{on} \quad \Gamma_c \end{cases}, \tag{3}$$
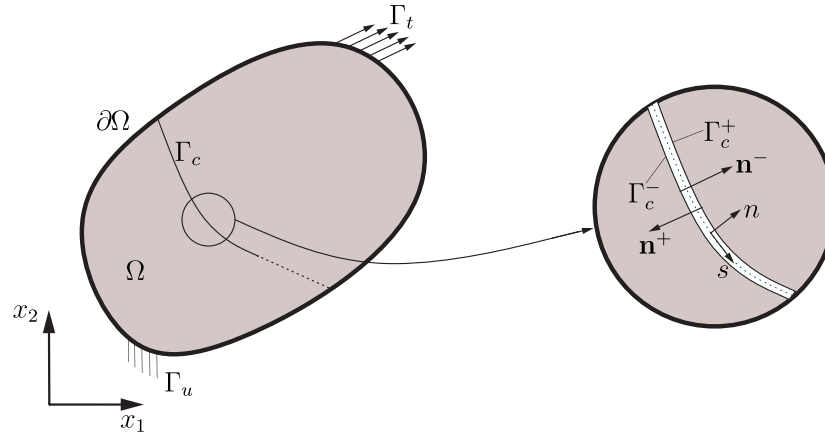
FIGURE 1 A domain Ω with an internal discontinuity Γ_c. The latter is represented as overlapping positive and negative sides, Γ_c^+ and Γ_c^-, respectively

where $\mathbf{n}$ denotes the normal vector at the boundaries, $\hat{\mathbf{u}}$ and $\hat{\mathbf{t}}$ represent the prescribed displacements and tractions, respectively, and $\boldsymbol{\sigma}$ is the Cauchy stress tensor, which relates to $\boldsymbol{\varepsilon}$ as

$$\boldsymbol{\sigma} = \mathbf{D}\boldsymbol{\varepsilon} \tag{4}$$

with $\mathbf{D}$ the fourth-order elastic stiffness tensor.

The traction $\mathbf{t}$ in the global coordinate system (x_1, x_2) is obtained from the traction $\mathbf{t}_d$ in the local coordinate system via a standard transformation:

$$\mathbf{t} = \mathbf{R}^{\mathrm{T}}\mathbf{t}_d. \tag{5}$$

The traction-opening relation

$$\mathbf{t}_d = \mathbf{t}_d \left([\![\boldsymbol{v}]\!] \right) \tag{6}$$

sets the relation between the traction acting at Γ_c and the displacement jump across it. A range of different traction-opening relations have been proposed, with applications ranging from ductile to quasibrittle fracture. Important parameters are the fracture strength t_u, which is the maximum traction that can be exerted on the interface Γ_c, and the fracture energy $\mathcal{G}_c$, which is the amount of energy that is needed to create a unit area of cracked surface, but also the shape of the decohesion curve can significantly affect the fracture process.

3 | NURBS REPRESENTATION OF A SOLID WITH A PREDEFINED INTERFACE

In the present study, NURBS basis functions are used to describe the geometry of the solid. This conforms well to the modelling technique used in CAD,[46] and in an isoparametric sense, they can be used to interpolate the displacement field $\mathbf{u}$:

$$\mathbf{x}\left(\xi^1, \xi^2\right) = \sum_{I=1}^{n_c} N_I\left(\xi^1, \xi^2\right) \mathbf{X}_I \qquad \mathbf{u}\left(\xi^1, \xi^2\right) = \sum_{I=1}^{n_c} N_I\left(\xi^1, \xi^2\right) \mathbf{U}_I, \tag{7}$$

where $\mathbf{X}_I$ represents the coordinates of the control points, $\mathbf{U}_I$ denotes the degrees of freedom at the control points, and n_c is the total number of control points. The NURBS basis function $N_I\left(\xi^1, \xi^2\right)$ is defined as

$$N_I\left(\xi^1, \xi^2\right) = \frac{N_i^p\left(\xi^1\right) N_j^q\left(\xi^2\right) w_{ij}}{W\left(\xi^1, \xi^2\right)} \tag{8}$$

with

$$W\left(\xi^1, \xi^2\right) = \sum_{i=1}^{n} \sum_{j=1}^{m} N_i^p\left(\xi^1\right) N_j^q\left(\xi^2\right) w_{ij} \tag{9}$$
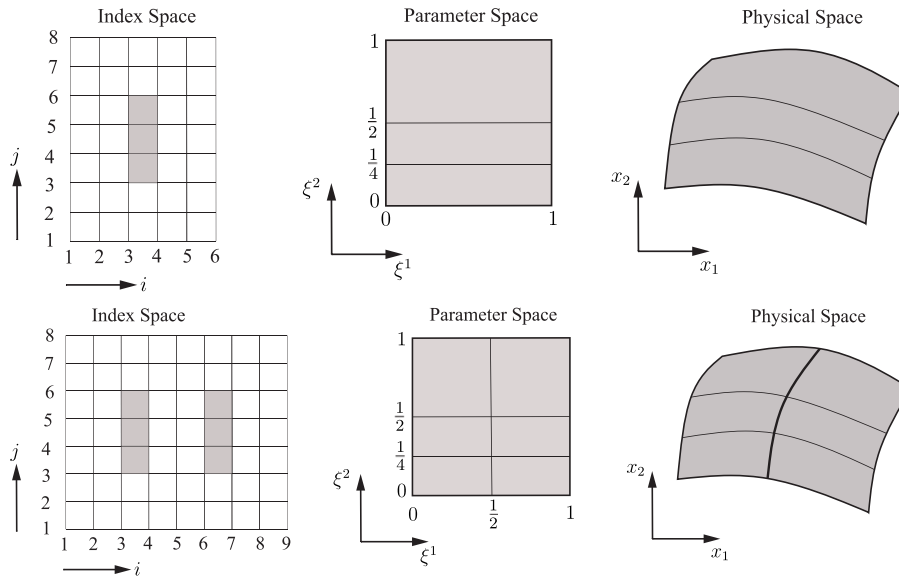
FIGURE 2 NURBS patch without (top) and with (bottom) crack interface Γ_c. The knot vectors for the top patch are $\Xi_1 = \{0,0,0,1,1,1\}$ and $\Xi_2 = \{0,0,0,0.25,0.5,1,1,1\}$. For the bottom patch, the knot vectors read $\Xi_1 = \{0,0,0,0.5,0.5,0.5,1,1,1\}$ and $\Xi_2 = \{0,0,0,0.25,0.5,1,1,1\}$

and w_{ij} weight factors. The index I is a function of the indices i and j of the univariate B-spline basis functions N_i^p and N_j^q.[47] N_i^p and N_j^q are piecewise polynomials of order p, respectively q, defined over a nondecreasing knot vector Ξ_1:

$$\Xi_1 = \left\{ \xi_1^1, \quad \xi_2^1, \quad \cdots, \quad \xi_{n+p+1}^1 \right\}. \tag{10}$$

The non-zero knot intervals in Ξ_1 can be conceived as elements. If the knot value ξ_i^1 is repeated, the multiplicity of ξ_i^1 is denoted by m_i. Because of this multiplicity, the basis function N_i^p becomes C^{p-m_i} continuous, which means that N_i^p is $p-m_i$ times continuously differentiable over the knot i. Depending on the values of p and m_i, higher-order or lower-order continuity can be achieved. This is beneficial for solving higher-order differential equations, eg, in previous studies,[48-54] but is also useful to insert an interface $\Gamma_c\left(\xi_d^1, \quad \xi^2\right)$ in the model,[26] see Figure 2. The interface is defined along the parametric direction ξ^2 at $\xi^1 = \xi_d^1$, and knot insertion is carried to increase the multiplicity of ξ_d^1 to $m_d = p + 1$, which yields C^{-1}-continuous basis functions.

The NURBS basis functions are defined over an entire patch, Figure 2. It is, however, convenient to directly incorporate NURBS in a standard finite element data structure, and the use of Bézier extraction has enabled this by representing the NURBS basis functions as element-wise Bernstein shape functions[32]:

$$\mathbf{N}^e = \mathbf{W}^e \mathbf{C}^e \frac{\mathcal{B}}{W^e} \qquad \text{with} \qquad W^e = (\mathbf{w}^e)^{\mathrm{T}} \mathbf{C}^e \mathcal{B}, \tag{11}$$

where $\mathbf{N}^e$ denotes the element-specific NURBS basis function, $\mathbf{C}^e$ represents the element-specific Bézier extraction operator, $\mathcal{B}$ contains the element-local Bernstein shape functions, $\mathbf{w}^e$ is the element weight vector, and $\mathbf{W}^e$ is the diagonal matrix of element weights.

3.1 | Isogeometric finite element discretisation

To solve Equation 3, it is first cast in its weak form, resulting in

$$\int_\Omega \delta\boldsymbol{\varepsilon} : \boldsymbol{\sigma} \mathrm{d}\Omega + \int_{\Gamma_c} \delta \llbracket \mathbf{u} \rrbracket \cdot \mathbf{t}(\llbracket \mathbf{u} \rrbracket) \mathrm{d}\Gamma = \int_{\Gamma_t} \delta \mathbf{u} \cdot \hat{\mathbf{t}} \mathrm{d}\Gamma \qquad \forall \delta \mathbf{u} \in v_0, \tag{12}$$

where $\delta\boldsymbol{\varepsilon}$, $\delta\mathbf{u}$, and $\delta \llbracket \mathbf{u} \rrbracket$ are the virtual strain, virtual displacement, and virtual relative displacement, respectively. The solution $\mathbf{u}$ belongs to the function space v:

$$v = \left\{ \boldsymbol{v} : v_i \in H^1(\Omega), v_i | \Gamma_D = \hat{u}_i \right\} \qquad v_0 = \left\{ \boldsymbol{v} : v_i \in H^1(\Omega), v_i | \Gamma_D = 0 \right\} \tag{13}$$

in which H^1 denotes the first-order Sobolev space.

Considering the kinematic relation, Equation 1, and the NURBS approximation, Equation 7, the weak form, Equation 12, yields a set of non-linear equations:

$$\mathbf{f}_{\text{int}}(\mathbf{u}) = \mathbf{f}_{\text{ext}} \tag{14}$$

with

$$\mathbf{f}_{\text{int}}(\mathbf{u}) = \int_{\Omega} \mathbf{B}^{\text{T}} \sigma \mathrm{d}\Omega + \int_{\Gamma_c} \mathbf{H}^{\text{T}} \mathbf{t}([\![\mathbf{u}]\!]) \, \mathrm{d}\Gamma \qquad \mathbf{f}_{\text{ext}} = \int_{\Gamma_t} \mathbf{N}^{\text{T}} \hat{\mathbf{t}} \mathrm{d}\Gamma. \tag{15}$$

The matrices $\mathbf{N}, \mathbf{B}$, and $\mathbf{H}$ contain the shape functions, their derivatives, and the relative displacements, respectively.[26] Linearisation yields the tangential stiffness matrix:

$$\mathbf{K}_{\text{tan}} = \mathbf{K}_{\text{bulk}} + \mathbf{K}_{\text{int}} = \int_{\Omega} \mathbf{B}^{\text{T}} \mathbf{D} \mathbf{B} \mathrm{d}\Omega + \int_{\Gamma_c} \mathbf{H}^{\text{T}} \mathbf{R}^{\text{T}} \mathbf{T}_d \mathbf{R} \mathbf{H} \mathrm{d}\Gamma \tag{16}$$

with $\mathbf{K}_{\text{bulk}}$ and $\mathbf{K}_{\text{int}}$ are tangential stiffness contributions from the bulk and the interface, respectively. The tangent stiffness of traction-opening law at the interface is given by[27]:

$$\mathbf{T}_d = \frac{\partial \mathbf{t}_d}{\partial [\![\nu]\!]}, \tag{17}$$

The sparsity pattern of the stiffness matrix, obtained when the unknowns are ordered in a "natural" manner, is shown in Figure 3. Figure 3A,B illustrates the sparsity pattern of the stiffness contribution of the bulk material. It is observed that the parts with bulk material are related in the absence of an interface. On the contrary, there is no connection between the left and right parts with the interface being in place. This connection is established through $\mathbf{K}_{\text{int}}$ as shown in Figure 3C. The resulting matrix $\mathbf{K}_{\text{tan}}$ is shown in Figure 3D.

4 | HIERARCHICAL REFINEMENT FOR COHESIVE CRACK GROWTH

Hierarchical B-splines were originally introduced for the local refinement of a surface,[55,56] and subsequently used in analysis. [57-68] To further improve the capability of hierarchical refinement truncated, hierarchical basis functions were proposed in previous studies.[69-72]

We will concisely discuss the fundamental idea of hierarchical basis function and the multilevel implementation of hierarchical refinement.[68] Then we will present the application of hierarchical refinement to cohesive crack growth.

4.1 | Hierarchical basis function

In this contribution, the hierarchical basis function is considered from an element-wise point of view, which fully conforms to the framework of Bézier extraction. The hierarchical basis function is defined over multiple hierarchy levels. The strong condition is assumed over the boundaries of different hierarchy levels,[60] which produces a nested hierarchical element structure. Here, we take an univariate NURBS to illustrate the construction of hierarchical basis functions. Because of the tensor product structure, the multivariate case can be deduced in straightforward manner.

First, we construct a hierarchy of P levels. The basis functions at each hierarchy level are defined over a knot vector Ξ^i ($i = 0, 1, \ldots P - 1$) with the same polynomial degree p, and Ξ^i is obtained by successive uniform knot insertions within Ω_d from initial knot vector Ξ^0. The univariate parametric domain is denoted by Ω_d. Subsequently, one obtains nested parametric domains $\Omega_d^i \subset \Omega_d^{i+1}$ and nested knot vectors $\Xi^i \subset \Xi^{i+1}$, Figure 4A. Each knot vector Ξ^i defines a set of NURBS basis functions $\mathbf{N}^i = \left\{ N_j^i \right\}_{j=1}^{n_i}$, which forms a nested NURBS approximation space $\mathcal{N}^i$. Because of the nested nature of $\mathcal{N}^i$, the basis function of hierarchy level i can be described by basis functions at hierarchy level j:

$$\mathbf{N}^i = \mathbf{S}^{i,j} \mathbf{N}^j = \prod_{l=i}^{j-1} \mathbf{S}^{l,l+1} \mathbf{N}^{l+1} \tag{18}$$

with $\mathbf{S}^{l,l+1}$ the subdivision or refinement operator.[68] It is noted that $\mathbf{S}^{l,l+1}$ is very sparse. An example of the NURBS subdivision is shown in Figure 4B, where each NURBS basis function of hierarchy level 0 has been expressed as a linear combination of the NURBS basis function of hierarchy level 1. The entries in $\mathbf{S}^{l,l+1}$ are defined as
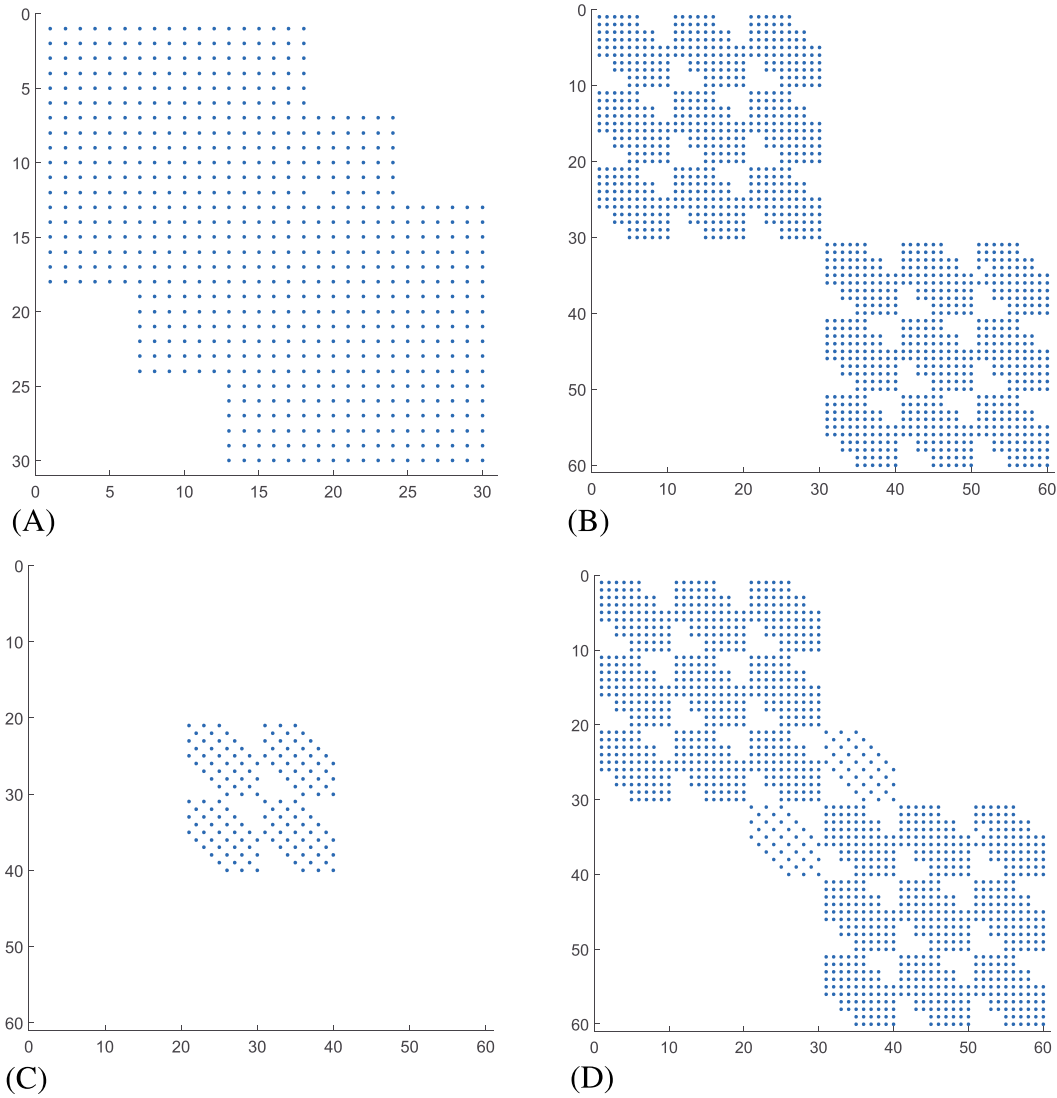
FIGURE 3 Sparsity pattern of the stiffness matrix with and without interface Γ_c for the NURBS patch of Figure 2: A, sparsity pattern of stiffness matrix of the bulk material without Γ_c; B, sparsity pattern of stiffness matrix of the bulk material with Γ_c; C, sparsity pattern of stiffness matrix $\mathbf{K}_{int}$; D, sparsity pattern of the composite stiffness matrix $\mathbf{K}_{tan}$

$$S^{l,l+1}_{IJ} = \frac{w^l_I}{w^{l+1}_J} M^{l,l+1}_{IJ} \tag{19}$$

with w^l_I the weight factor of the Ith basis function on hierarchy level l, and $M^{l,l+1}_{IJ}$ is an entry in the linear subdivision or refinement operator for the B-spline basis functions of hierarchy level l and $l + 1$.[73] The B-spline basis functions of hierarchy level l and $l + 1$ are defined by the knot vectors Ξ^l and Ξ^{l+1} with weight factor $w = 1$.

To construct the hierarchical basis function space $\mathcal{A}$, the active elements and the basis functions in the multilevel hierarchy must be identified. The active element is chosen by a marking criterion, for instance an a posteriori error estimator.[72] It is defined across different hierarchy levels without overlap or gap, Figure 5A. The parametric domain of active elements

$$\Omega_d = \bigcup_{i=0}^{P-1} E^i_A \qquad \text{with} \qquad E^i_A = \bigcup_e \Omega^{e,i}_d \tag{20}$$

is plotted in green, and P is the number of hierarchy levels. Further, E^i_A represents the parametric domain of all active elements on hierarchy level i, and $\Omega^{e,i}_d$ denotes the parametric domain of the element e on hierarchy level i.
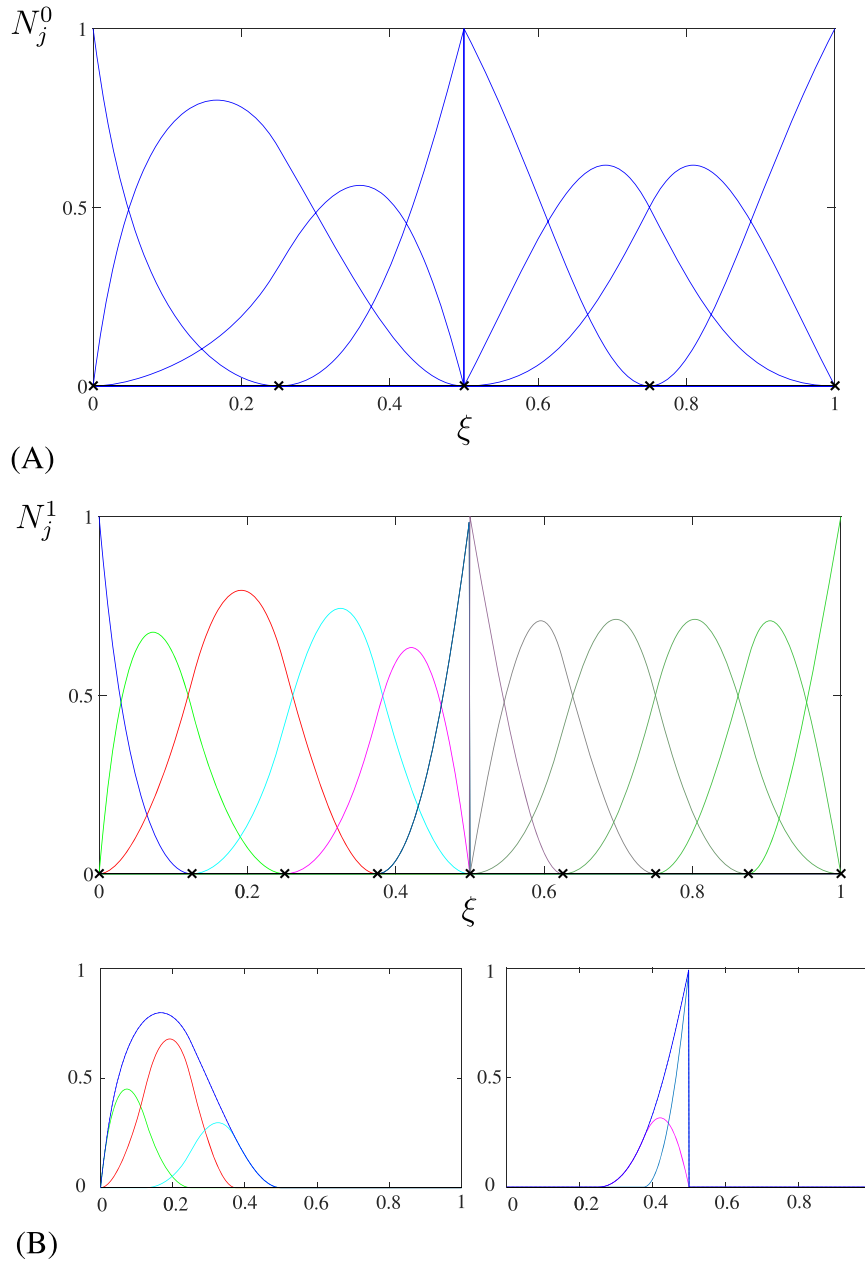
FIGURE 4 A, Basis functions and meshes for a hierarchy of 2 levels: B, examples of a subdivision of NURBS basis functions, which is a linear combination of refined basis functions. The knot vector of hierarchy level 0 is $\Xi^0 = \{0, 0, 0, 0.25, 0.5, 0.5, 0.5, 0.75, 1, 1, 1\}$. The weight factor of the basis function of hierarchy level 0 is $w^0 = \{1, 2, 1, 1, 1, 0.5, 0.5, 1\}$. The NURBS basis functions of hierarchy level 1 are obtained by successive uniform knot insertion into Ξ^0. The knots at each hierarchy level are indicated by ×

Next, a linearly independent hierarchical basis function space $\mathcal{A}$ can be defined. This space will be used to describe the geometry of the solid and to approximate the solution space. We will take an element-based selection approach to construct $\mathcal{A}$ as in Hennig et al[68] and illustrate this concept by introducing two additional parametric domains for hierarchy level l:

$$\Omega_d^{l+} = \bigcup_{i=l+1}^{P-1} E_A^i \qquad \Omega_d^{l-} = \bigcup_{i=0}^{l-1} E_A^i. \tag{21}$$

With the parametric domains Ω_d, Ω_d^{l+}, and Ω_d^{l-}, 3 sets of basis function space are defined:
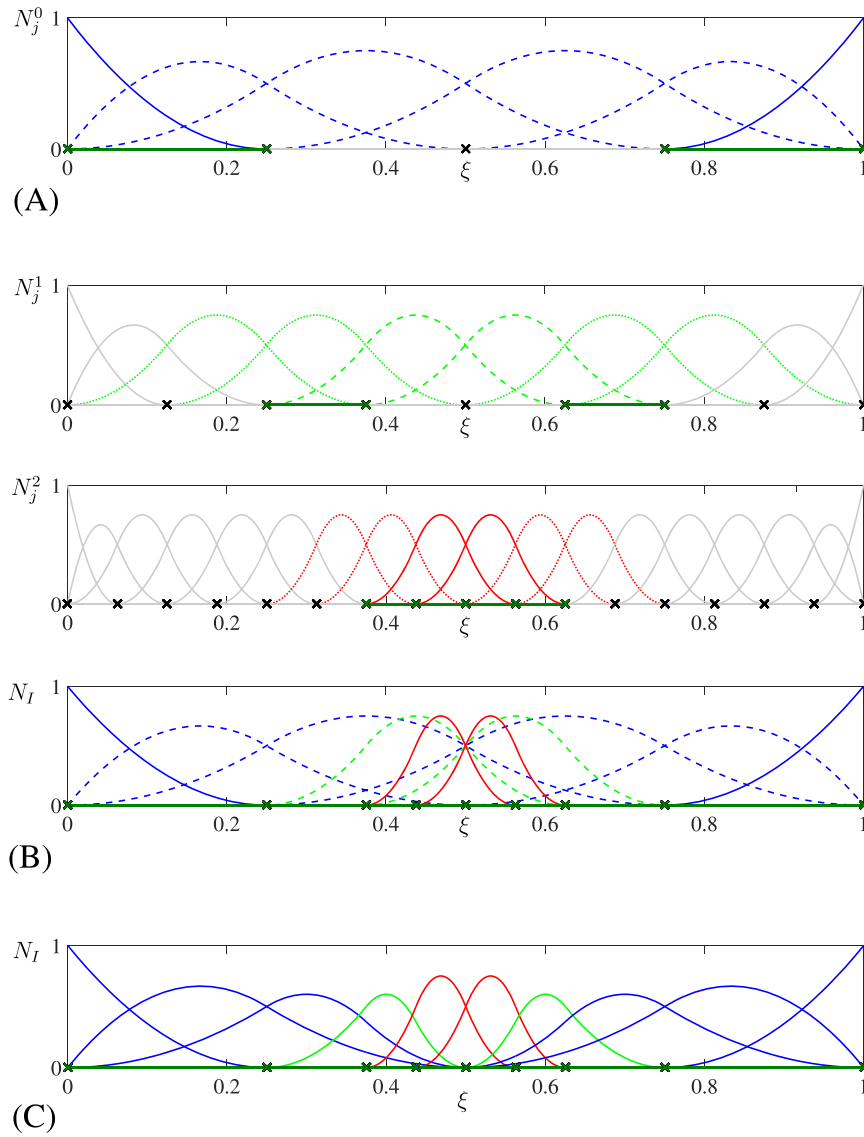
FIGURE 5 Definition of the basis function space; A, illustration of basis function sets $\mathcal{A}^l$, $\mathcal{A}^l_-$, and $\mathcal{A}^l_+$; B, final hierarchical basis functions; C, final truncated hierarchical basis functions

$$\begin{cases} \mathcal{A}^l = \left\{ N_j^l \in \mathcal{N}^l : \sup N_j^l \bigcap E_A^l \neq \emptyset \right\} \\ \mathcal{A}_+ = \bigcup_{l=0}^{P-1} \mathcal{A}_+^l \quad \text{with} \quad \mathcal{A}_+^l = \left\{ N_j^l \in \mathcal{A}^l : \sup N_j^l \bigcap \Omega_d^{l+} \neq \emptyset \right\} \\ \mathcal{A}_- = \bigcup_{l=0}^{P-1} \mathcal{A}_-^l \quad \text{with} \quad \mathcal{A}_-^l = \left\{ N_j^l \in \mathcal{A}^l : \sup N_j^l \bigcap \Omega_d^{l-} \neq \emptyset \right\}. \end{cases} \tag{22}$$

Herein, $\mathcal{A}^l$ is the union of basis functions defined over the active elements on hierarchy level l, see Figure 5A. $\mathcal{A}_+^l$ denotes the basis functions in $\mathcal{A}^l$ with support over the active elements on finer hierarchy levels, which is plotted in dashed lines, Figure 5A. $\mathcal{A}_-^l$ represents the basis functions in $\mathcal{A}^l$ with support over the active elements on coarser hierarchy levels, which is indicated by dotted lines in Figures 5A. Finally, the definition of hierarchical basis function space $\mathcal{A}$ is given as

$$\mathcal{A} = \bigcup_{l=0}^{P-1} \mathcal{A}_a^l \qquad \text{with} \qquad \mathcal{A}_a^l = \mathcal{A}^l \setminus \mathcal{A}_-^l, \tag{23}$$

where "\" is the logic NOT; $\mathcal{A}_a^l$ denotes the active basis functions of hierarchy level l, Figure 5B. $\mathcal{A}$ denotes the standard hierarchical basis function space.[60]

From linear combinations of basis functions at hierarchy levels l and $l + 1$, we can obtain a so-called truncated hierarchical basis function space,[69] see Figure 5C:

$$\mathcal{A}_T = \bigcup_{l=0}^{P-1} \mathcal{A}_{T,a}^l \quad \text{with} \quad \mathcal{A}_{T,a}^l = \left\{ \tau_i^l \in \mathcal{A}_a^l : \sup \tau_i^l \nsubseteq E_A^{l+1} \right\}, \tag{24}$$

where

$$\tau_i^l = \left\{ \tau_i^l \in \mathcal{N}^l : \tau_i^l = \sum S_{ij}^{l,l+1} N_j^{l+1} \right\}, \tag{25}$$

see Equation 18. In general, standard hierarchical basis functions do not satisfy the partition of unity property, which is different for the truncated hierarchical basis functions, which do fulfill this property.

4.2 | Multilevel implementation of hierarchical basis function

With the active elements and basis functions defined in Section 4.1, the stiffness matrix can be computed in a multilevel adaptivity approach.

First, the stiffness matrix of active elements at each hierarchy level is computed by using Bézier extraction, without considering possible interaction between the multilevel basis functions. After assembly of the stiffness matrix at each level, the global system of equations follows as

$$\mathbf{K}\mathbf{U} = \mathbf{F}, \tag{26}$$

where $\mathbf{U}$ includes the nodal degrees of freedom at each hierarchy level, $\mathbf{F}$ represents the force vector, $\mathbf{K}$ is a sparse matrix with the submatrices $\mathbf{K}^i$ along the diagonal, Figures 6A and 7A. The stiffness submatrix $\mathbf{K}^i$ is built from the active elements at hierarchy level i and is a square sparse matrix of $2n_c^i \times 2n_c^i$, with n_c^i the number of control points at hierarchy level i. It is noted that $\mathbf{K}^i$ also has a high degree of sparsity, see Figures 6A and 7A. The empty spaces in $\mathbf{K}^i$ reflect that there is no contribution from the inactive elements at level i.

Equation 26 does not consider the interaction between the multilevel hierarchical basis functions. This interaction is incorporated in the analysis by the hierarchical subdivision operator $\mathbf{M}_h$. The final hierarchical system of equation then reads

$$\mathbf{K}_h\mathbf{U}_h = \mathbf{F}_h \quad \text{with} \quad \mathbf{K}_h = \mathbf{M}_h\mathbf{K}\mathbf{M}_h^{\mathrm{T}} \quad \text{and} \quad \mathbf{F}_h = \mathbf{M}_h\mathbf{F}. \tag{27}$$

The sparsity of $\mathbf{K}_h$ is shown in Figures 6C and 7C. There are many zero entries in $\mathbf{K}_h$ because of the multilevel interaction of the hierarchical basis functions and the inactive elements at each level, which renders it singular. To regularise this, $\mathbf{K}_h$ can be restructured according to the active basis function space $\mathcal{A}$ or $\mathcal{A}_T$, yielding a resized $\mathbf{K}_h$-matrix.[68] Alternatively, $\mathbf{K}_h$ can be kept constant in size, adding units on the main diagonal at the zero entries, red stars in Figures 6D and 7D. This approach will only marginally increase the memory requirement for storing $\mathbf{K}_h$.

The hierarchical subdivision operator $\mathbf{M}_h$ is defined as

$$\mathbf{M}_h = \begin{bmatrix} \mathbf{I}^0 & \hat{\mathbf{M}}^{0,1} & \hat{\mathbf{M}}^{0,2} & \dots & \hat{\mathbf{M}}^{0,P-1} \\ & \mathbf{I}^1 & \hat{\mathbf{M}}^{1,2} & \dots & \hat{\mathbf{M}}^{1,P-1} \\ & & \mathbf{I}^2 & \dots & \hat{\mathbf{M}}^{2,P-1} \\ & & & \ddots & \\ \mathbf{0} & & & & \mathbf{I}^{P-1} \end{bmatrix} \tag{28}$$

with

$$I_{IJ}^l = \begin{cases} 1 & \text{for} \quad I = J \quad \text{and} \quad N_I^l \in \mathcal{A}_a^l \\ 0 & \text{else} \end{cases}. \tag{29}$$

The subdivision operator $\hat{\mathbf{M}}^{l,k}$ in Equation 28 is defined for standard hierarchical basis function and for truncated hierarchical basis function, respectively. For standard hierarchical basis function, it is given by

$$\hat{M}_{IJ}^{l,k} = \begin{cases} S_{IJ}^{l,k} & \text{for} \quad N_I^l \in \mathcal{A}_+^l \\ 0 & \text{else} \end{cases}, \tag{30}$$

where $S_{IJ}^{l,k}$ is defined in Equation 18. For truncated hierarchical basis function, the entries of $\hat{\mathbf{M}}^{l,k}$ are given by
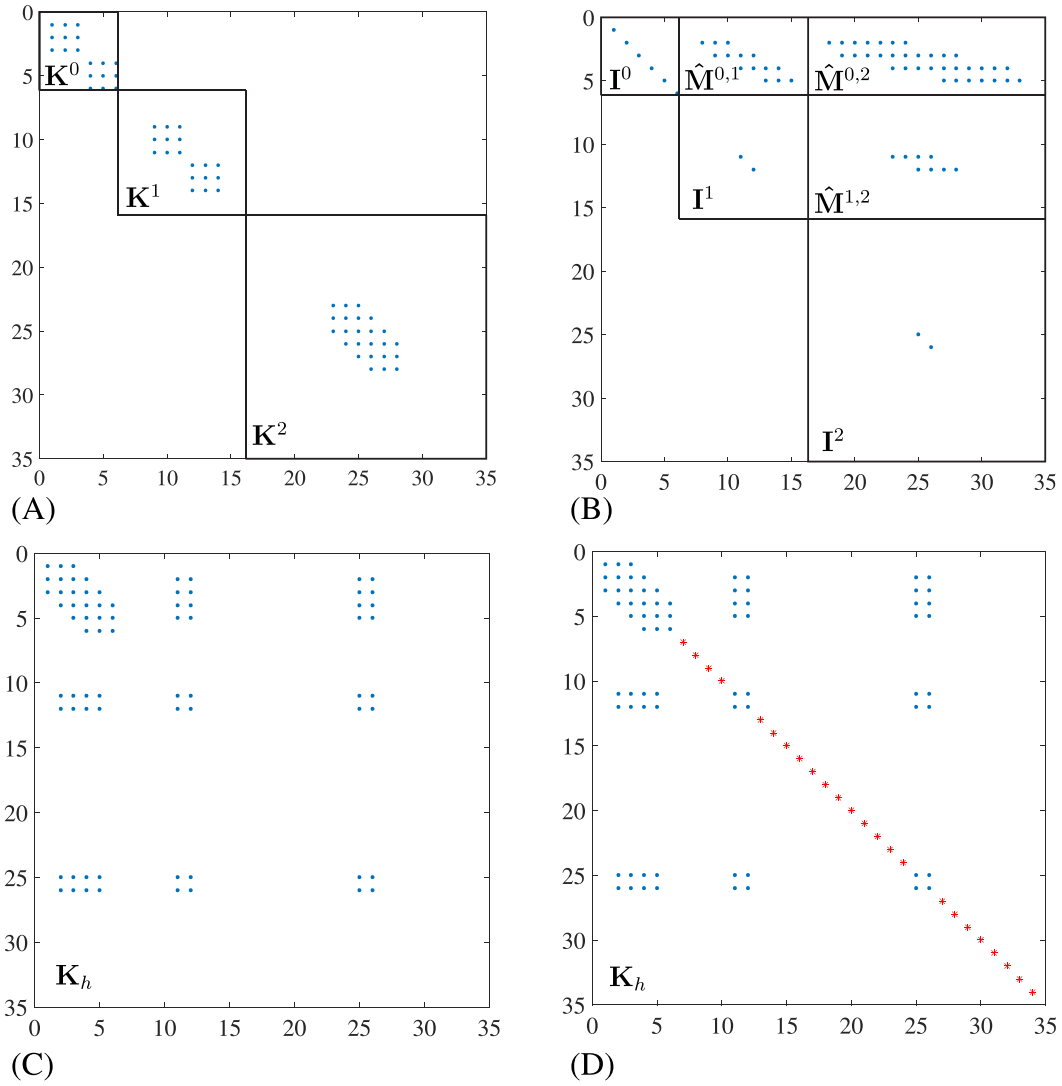
FIGURE 6 Sparsity pattern of the stiffness matrix and the hierarchical subdivision operator generated by the standard hierarchical basis function in Figure 5B: A, $\mathbf{K}$ from Equation 26; B, hierarchical subdivision operator; C, hierarchical stiffness matrix $\mathbf{K}_h$; D, final hierarchical stiffness matrix (the red stars represent the supplementary identity terms)

$$
\hat{M}_{IJ}^{l,k} = \begin{cases} S_{IJ}^{l,k} & \text{for} \quad N_I^l \in \mathcal{A}_+^l \quad \text{and} \quad N_J^k \in \mathcal{A}_-^k \\ 0 & \text{else} \end{cases}. \tag{31}
$$

The solution of Equation 27 yields the displacement $\mathbf{U}_h$ for the control points associated with the hierarchical basis functions. In a non-linear calculation, computation of the stiffness matrix $\mathbf{K}$ requires the displacement vector $\mathbf{U}$ rather than $\mathbf{U}_h$ from the previous iteration, see Equation 26, and is obtained as

$$
\mathbf{U} = \mathbf{M}_h^{\mathrm{T}} \mathbf{U}_h. \tag{32}
$$

4.3 │ Adaptive hierarchical refinement for cohesive crack growth

To decide on local, adaptive refinement, and coarsening, we use $[\![v^c]\!]$, which is defined as

$$
[\![v^c]\!] = \begin{cases} [\![v_n]\!] & \text{mode-I cracking} \\ [\![v_s]\!] & \text{mode-II cracking} \\ \sqrt{[\![v_n]\!]^2 + \beta^2 [\![v_s]\!]^2} & \text{mixed-mode cracking} \end{cases} \tag{33}
$$

with β a mode-mixity parameter. Using $[\![v^c]\!]$, element refinement and coarsening are then decided according to the following:
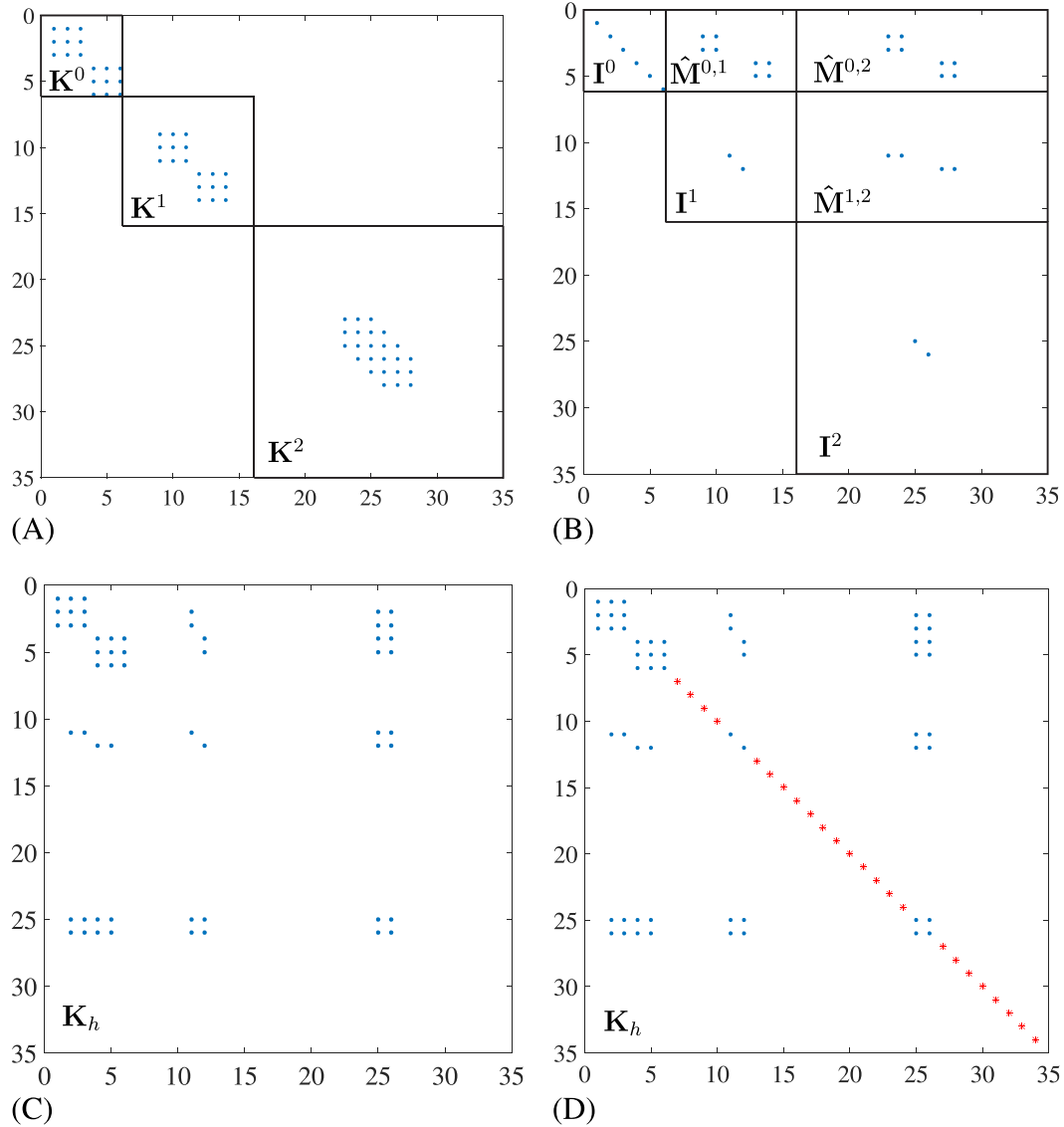
FIGURE 7 Sparsity pattern of the stiffness matrix and hierarchical subdivision operator generated by the truncated hierarchical basis function in Figure 5C. The caption of each subfigure is the same as Figure 6

1. $\delta_1 \leqslant [\![v^c]\!] \leqslant \delta_2$ Mark the elements adjacent to the interface Γ_c for refinement.
2. $[\![v^c]\!] \geqslant \delta_m$ Mark the elements adjacent to the interface Γ_c for coarsening.

Two special conditions can occur:

1. If an element marked for refining is at the highest hierarchy level, no further refinement will take place; the element will not be marked to be refined.
2. Conversely, if an element marked for coarsening is at the first hierarchy level, no further local coarsening will occur.

The steps for the adaptive hierarchical refinement for cohesive crack growth can be summarised as follows:

$\mathcal{S}1$ Solve Equation 27 for the displacements $\mathbf{U}_h$ and then compute $\mathbf{U}$ through Equation 32.

To properly take into account the Dirichlet boundary condition, the displacement boundary condition must be modified such that

$$U_I = \begin{cases} \hat{U}_I & \text{on} \quad \Gamma_u \quad \text{when} \quad N_I \in \mathcal{A} \quad \text{or} \quad \mathcal{A}_T \\ \mathbf{0} & \text{on} \quad \Gamma_u \quad \text{else} \end{cases} . \tag{34}$$

$\mathcal{S}2$ Compute the jump $[\![v]\!]$ at the interface Γ_c from Equations 1, 2, and 7.
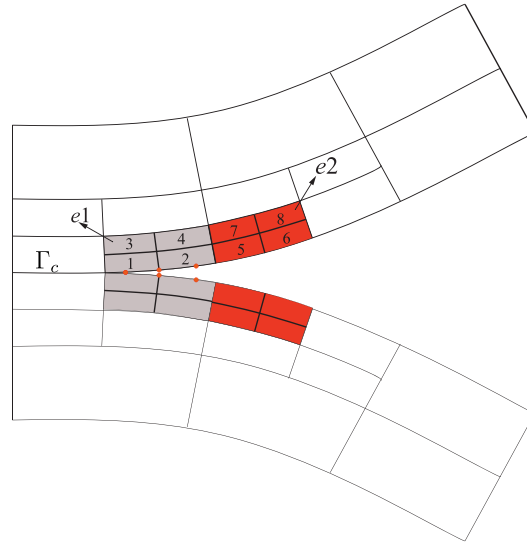
FIGURE 8 Refinement and coarsening along the interface Γ_c. Here, we refer to elements (1, 2, 3, 4) as the child elements of element $e1$, or vice versa, to element $e1$ as the parent element of elements (1, 2, 3, 4). The same applies to element $e2$ and the elements (5, 6, 7, 8)

The opening $[\![v]\!]$ at the interface Γ_c is evaluated at the integration points, which are used to compute $\mathbf{K}_{\text{int}}$ in Equation 16. In Figure 8, the integration points are denoted by red circles. Herein, full Gaussian quadrature is used, which involves $p + 1$ integration points per element along the interface (p denotes the polynomial degree of the NURBS basis function).

$\mathcal{S}3$ Check whether $[\![v^c]\!]$ is within a range $[\delta_1, \quad \delta_2]$ or bigger than δ_m.

If $[\![v^c]\!]$ of any integration point in an element meets the condition $\delta_1 \leqslant [\![v^c]\!] \leqslant \delta_2$, the element will be refined. The refinement of a single element will lead to 2 active child elements per parametric direction, see Figure 8. In this figure, element $e1$ must to be refined, which yields 4 child elements (1, 2, 3, 4).

If $[\![v^c]\!]$ of all integration points of an element satisfy $[\![v^c]\!] \geqslant \delta_m$, the element E_{adj} will be coarsened. Henceforth, we denote the parent element of E_{adj} as E_p. To maintain the nested structure, it must be checked whether all child elements of E_p at the interface Γ_c need to be coarsened. Consider Figure 8, for example. After evaluation of $[\![v^c]\!]$, element 5 is marked for coarsening. Therefore, it is also checked whether element 6 should be coarsened as well, since both arise from the same parent element ($e2$). In this case, both elements (5 and 6) will be coarsened.

$\mathcal{S}4$ Refine or coarsen the marked elements. If no element is required to be refined or coarsened, stop the calculation, otherwise return to $\mathcal{S}1$.

Remark. To obtain a well-conditioned stiffness matrix $\mathbf{K}_h$ in Equation 27, for the element refinement and coarsening, the adjacent elements are forced to be from the same, or at most from 2 consecutive hierarchy levels.

5 | IMPLEMENTATION ASPECTS

Having derived the formulation for the adaptive hierarchical refinement for cohesive crack growth, we now outline the implementation aspects in the context of an isogeometric analysis framework. First, we introduce the data structure. Then the refinement procedure will be described in detail. Finally, we will provide the mapping of the displacement vector and the history variables for the newly activated elements. To preserve transparency, we will focus on a two-dimensional case.

5.1 | Data structures

We adopt an element-wise point of view for the implementation and consider a hierarchy of P levels. Initially, the following 3 data sets will be considered and saved:

1. The knot vector $\left(\Xi_1^I, \quad \Xi_2^I\right)$ and the control points $\mathbf{P}^I$ on each hierarchy level are defined by successive uniform knot insertion starting from the initial knot vector $\left(\Xi_1^0, \quad \Xi_2^0\right)$ and the initial control points $\mathbf{P}^0$, which can be inferred from the CAD model. Using $\left(\Xi_1^I, \quad \Xi_2^I\right)$, the basis functions can be constructed for each hierarchy level.
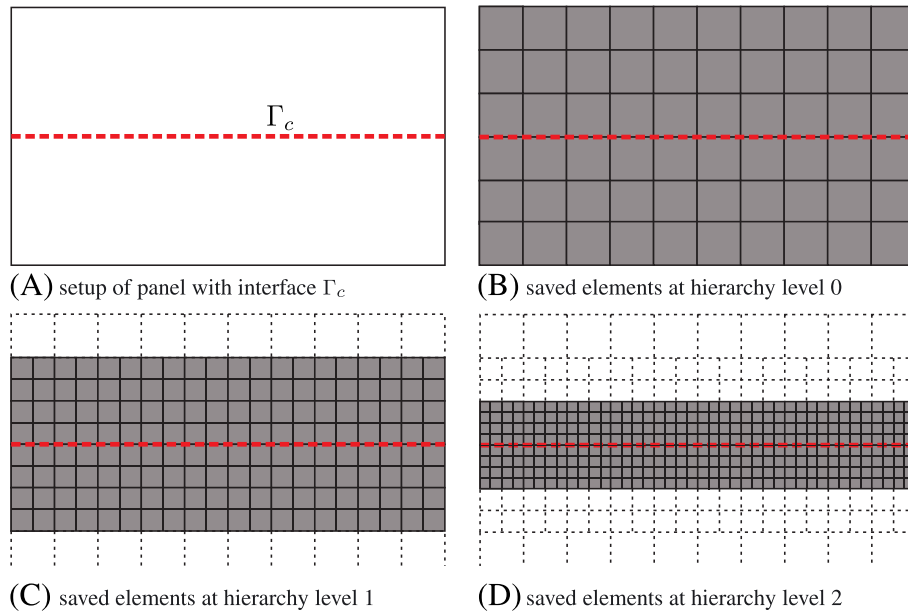
FIGURE 9 Saved elements at each hierarchy level. In this example, 3 hierarchy levels are considered

2. Given the knot vector $\left(\Xi_1^I, \Xi_2^I\right)$, the elements and corresponding Bézier extractor in Equation 11 are obtained for each hierarchy level. The parent-child relation between elements on different hierarchy levels are determined.
3. The subdivision operator $\mathbf{S}^{l,l+1}$ is computed from Equation 19. Here, we only retain the subdivision operator between 2 consecutive hierarchy levels.

Since the crack propagates along the interface Γ_c, element refinement and coarsening will occur at the elements adjacent to Γ_c. To reduce the storage of these data sets, we will only keep the 4 elements adjacent to Γ_c for hierarchy level higher than 0 and store their data, see Figure 9. Because of the reduced number of elements in storage, the degrees of freedom in Equations 26 and 27 will also be reduced.

In the refinement process, 2 sets of boolean vectors are defined to indicate the state of the elements—active or inactive—at each hierarchy level. The length of these vectors is n_{eT}, which is the total number of elements at the P hierarchy levels. They are initialised as **false**:

1. $\mathbf{E}_a$: indicator of active elements. $\mathbf{E}_a^i = \{\mathbf{true} : \quad \text{element } i \text{ is } \mathbf{active}\}$.
2. $\mathbf{E}_{ac}$: indicator of active child elements. $\mathbf{E}_{ac}^i = \{\mathbf{true} : \text{child elements of element } i \text{ are } \mathbf{active}\}$.

On the basis of $\mathbf{E}_a$ and $\mathbf{E}_{ac}$, 3 sets of boolean vectors are obtained, which indicate the active and inactive state of basis functions at each hierarchy level. The length of the vectors is n_{bT}, which equals the total number of basis functions at the P hierarchy levels. They are initialised as **false**. Further, we define the basis functions at the P hierarchy levels as $\mathbf{N} = \{N^i\}, \quad (i = 1, 2, \cdots, n_{bT})$:

1. $\mathbf{A}_a$: indicator of the basis function in the space of hierarchical basis functions $\mathcal{A}$ or $\mathcal{A}_T$. $\mathcal{A}$ and $\mathcal{A}_T$ are obtained from Equations 23 and 24, respectively. $\mathbf{A}_a^i = \{\mathbf{true} : N^i \in \mathcal{A} \quad \text{or} \quad \mathcal{A}_T\}$.
2. $\mathbf{A}_-$: indicator of the basis function in the set $\mathcal{A}_-$, Equation 22. $\mathbf{A}_-^i = \{\mathbf{true} : N^i \in \mathcal{A}_-\}$.
3. $\mathbf{A}_+$: indicator of the basis function in the set $\mathcal{A}_+$, Equation 22. $\mathbf{A}_+^i = \{\mathbf{true} : N^i \in \mathcal{A}_+\}$.

To obtain the hierarchical system of Equation 27, one needs to compute $\mathbf{M}_h$ in Equation 28. $\mathbf{M}_h$ will be saved in a sparse format. To obtain $\mathbf{M}_h$, the data sets $\mathbf{A}_a, \mathbf{A}_-, \mathbf{A}_+$ and $\mathbf{S}^{l,l+1}$ are used. A pseudocode to compute $\mathbf{A}_a, \mathbf{A}_-$, and $\mathbf{A}_+$ can be found in Hennig et al.[68]

5.2 | Refinement procedure

Based on the data structure of Section 5.1, the procedure for adaptive hierarchical refinement of cohesive crack growth has been developed and is shown in Algorithm 1.

Algorithm 1 Adaptive hierarchical refinement for cohesive crack growth

---

$\mathcal{S}1$ Read the geometry data to obtain the initial knot vector $\left(\Xi_0^1,\ \Xi_0^2\right)$ and the initial control points $\mathbf{P}_0$.

$\mathcal{S}2$ Carry out successive uniform knot insertion to generate $\left(\Xi_1^I,\ \Xi_2^I\right)$ and $\mathbf{P}^I$ for each hierarchy level I from $\left(\Xi_1^0,\ \Xi_2^0\right)$ and $\mathbf{P}^0$.

$\mathcal{S}3$ Compute the subdivision operator $\mathbf{S}^{l,l+1}$ between two consecutive hierarchy levels l and $l+1$.

$\mathcal{S}4$ Obtain the list of active elements and active child elements to compute $\mathbf{E}_a$ and $\mathbf{E}_{ac}$.

   For the first iteration, the active elements and active child elements are defined as those from previous load step, and for the first load step, the active elements are directly provided by the initial mesh.

$\mathcal{S}5$ Compute the boolean vectors $\mathbf{A}_a$, $\mathbf{A}_+$, $\mathbf{A}_-$ and the subdivision operator $\mathbf{M}_h$.

$\mathcal{S}6$ Apply the Newton-Raphson scheme to obtain $\mathbf{U}$.

$\mathcal{S}7$ Check whether each element should be refined or coarsened and mark it accordingly, see Algorithm 2.

   When there are no elements marked for refinement or coarsening, stop the calculation for the current load step and go to the next load step. Otherwise, obtain the new list of active elements and active child elements on the basis of the marked elements and return to $\mathcal{S}4$.

   When $\mathbf{U}$ has been computed, we can proceed to the kernel of adaptive hierarchical refinement: element refinement and coarsening. Herein, we will focus on element refinement and coarsening for crack growth, but this can be extended to other non-linearities, such as plasticity.

Algorithm 2 Element refinement and coarsening.

$\mathcal{R}C1$ Compute the opening $[\![v]\!]$ of each active element adjacent to the interface Γ_c, see Equation 2. $[\![v]\!]$ is evaluated at the integration points along Γ_c.

$\mathcal{R}C2$ Check whether $[\![v^c]\!]$ is within a range $[\delta_1,\ \delta_2]$ or beyond δ_m, see Equation 33. Mark the elements for refinement and coarsening.

$\mathcal{R}C3$ Refine the elements in order to get the new list of active elements and active child elements. Here, the elements to be refined are represented as E_r and all child elements of E_r as E_{rc}.

   ◦ Get the old list of active elements and active child elements, $\mathbf{E}_a$ and $\mathbf{E}_{ac}$.

   ◦ Set element E_r **inactive** in the list of active elements and $\mathbf{E}_a(E_r) =$ **false**. Set element E_r **active** in the list of active child elements and $\mathbf{E}_{ac}(E_r) =$ **true**.

   ◦ Set all child elements E_{rc} **active** in the list of active elements and $\mathbf{E}_a(E_{rc}) =$ **true**. Set E_{rc} **inactive** in the list of active child elements and $\mathbf{E}_{ac}(E_{rc}) =$ **false**.

$\mathcal{R}C4$ Coarsen the elements to make the updated list of active elements and active child elements, $\mathbf{E}_a$ and $\mathbf{E}_{ac}$. The elements to be coarsened are denoted by E_c, the parent element of E_c by E_p and all child elements of E_p by E_{Ac}.

   ◦ Obtain the list of active elements and active child elements after element refinement, $\mathbf{E}_a$ and $\mathbf{E}_{ac}$.

   ◦ Set the parent element E_p **active** in the list of active elements and $\mathbf{E}_a(E_p) =$ **true**. Set the parent element E_{gp} of E_p **active** in the list of active child elements and $\mathbf{E}_{ac}(E_{gp}) =$ **true**.

   ◦ Set all child elements E_{Ac} **inactive** in the list of active elements and $\mathbf{E}_a(E_{Ac}) =$ **false**. Set the parent element E_p **inactive** in the list of active child elements and $\mathbf{E}_{ac}(E_p) =$ **false**.

5.3 | Update of the displacement vector and the history variables

During refinement and coarsening, new elements are introduced in or deleted from the set of active elements. For non-linear problems, this requires a transfer of the displacements from the previous time step t to provide initial values for the new elements

at time step $t + \Delta t$. The transfer of the displacement vector from coarse elements to finer elements is exact. However, when transferring information from finer elements to coarser elements, information may be lost.

We consider ${}^t\mathbf{U}$, obtained at time step t. The corresponding hierarchical basis function spaces are ${}^t\mathcal{A}$ or ${}^t\mathcal{A}_T$. For the next time step $t + \Delta t$, certain elements can have been marked for refinement or coarsening, and elements will be activated or deactivated. As a consequence, their basis functions and control points will be also activated, or deactivated. We denote the space of the hierarchical basis functions at time step $t + \Delta t$ by ${}^{t+\Delta t}\mathcal{A}$, or ${}^{t+\Delta t}\mathcal{A}_T$.

In a non-linear solution scheme, we need to map the vector ${}^t\mathbf{U}$ at time step t so as to produce a new initial vector ${}^{t+\Delta t}_0\mathbf{U}$ at time step $t + \Delta t$. During element refinement, the mapping of ${}^t\mathbf{U}$ to ${}^{t+\Delta t}_0\mathbf{U}$ is exact and is given by

$$
{}^{t+\Delta t}_0\mathbf{U}^{l+1} = \left(\tilde{\mathbf{S}}^{l,l+1}\right)^{\mathrm{T}} {}^t\mathbf{U}^l, \tag{35}
$$

where l is the hierarchy level, and $\tilde{\mathbf{S}}^{l,l+1}$ denotes the modified subdivision operator, which is derived from Equation 19, as follows:

$$
\tilde{S}^{l,l+1}_{IJ} = \begin{cases} S^{l,l+1}_{IJ} & \text{for} \quad N^{l+1}_J \in {}^{t+\Delta t}\mathcal{A}^{l+1} \quad \text{or} \quad {}^{t+\Delta t}\mathcal{A}^{l+1}_T \\ 0 & \text{else} \end{cases}. \tag{36}
$$

During coarsening, information can be lost during the mapping of ${}^t\mathbf{U}$ to ${}^{t+\Delta t}_0\mathbf{U}$. Herein, a global least-squares fit is used to perform the mapping, which is achieved by minimising

$$
\psi = \int_\Omega \left\| {}^{t+\Delta t}_0\mathbf{u} - {}^t\mathbf{u} \right\| \mathrm{d}\Omega = \int_\Omega \left\| {}^{t+\Delta t}\mathbf{N}_A \; {}^{t+\Delta t}_0\mathbf{U} - {}^t\mathbf{u} \right\| \mathrm{d}\Omega \tag{37}
$$

in which $\mathbf{u}$ is the displacement, and ${}^{t+\Delta t}\mathbf{N}_A$ denotes the basis functions associated with the active elements at time step $t + \Delta t$. Minimising Equation 37 with respect to ${}^{t+\Delta t}_0\mathbf{U}$ yields

$$
\mathbf{M} \, {}^{t+\Delta t}_0\mathbf{U} = \mathbf{p} \tag{38}
$$

with

$$
\mathbf{M} = \int_\Omega \left({}^{t+\Delta t}\mathbf{N}_A \right)^{\mathrm{T}} {}^{t+\Delta t}\mathbf{N}_A \mathrm{d}\Omega, \tag{39}
$$

which is obtained directly by Gaussian quadrature at each active element at $t + \Delta t$, and

$$
\mathbf{p} = \int_\Omega \left({}^{t+\Delta t}\mathbf{N}_A \right)^{\mathrm{T}} {}^t\mathbf{u}\mathrm{d}\Omega = \int_{\Omega^t} \left({}^{t+\Delta t}\mathbf{N}_A \right)^{\mathrm{T}} \left({}^t\mathbf{N}_A \right) {}^t\mathbf{U}\mathrm{d}\Omega, \tag{40}
$$

where the integration is performed at each active element at t. ${}^t\mathbf{N}_A$ and ${}^{t+\Delta t}\mathbf{N}_A$ represent the basis functions associated with the active elements at t and $t + \Delta t$, respectively. An alternative approach to perform the mapping ${}^t\mathbf{U}$ to ${}^{t+\Delta t}_0\mathbf{U}$ during coarsening would be to exploit the pseudoinverse of the subdivision matrix.[74]

The introduction of new elements will also result in a new cohesive segment along the interface. Accordingly, the history parameters of the integration points along Γ_c need to be updated. Herein, for the refinement of cohesive segment, the history parameters are updated by an approach similar to that in Equation 35. During coarsening, this issue of updating the history variables is not encountered since full debonding will then already have taken place.

6 | NUMERICAL EXAMPLES

To investigate the performance of the approach, three examples are presented. In the examples, the truncated hierarchical basis function space $\mathcal{A}_T$ is used to describe the geometry of the solid and to span the solution space. The interface Γ_c is defined by NURBS basis functions, and knot insertion has been used to achieve C^{-1}-continuity. The Xu-Needleman cohesive zone relation has been used throughout to describe the adhesive fracture.[36]

During refinement, it must be checked whether $\delta_1 \leqslant [\![v^c]\!] \leqslant \delta_2$ or $[\![v^c]\!] > \delta_m$. To determine δ_1, δ_2, and δ_m, the crack mode indicated in Equation 33 should be considered. In this single mode crack growth, δ_1, δ_2, and δ_m are assumed to be

$$
\delta_1 = (0.5\,\delta_n \;\text{or}\; 0.5\,\delta_s), \qquad \delta_2 = (2\,\delta_n \;\text{or}\; 2\,\delta_s), \qquad \delta_m = (5\,\delta_n \;\text{or}\; 5\,\delta_s) \tag{41}
$$

in which δ_n and δ_s are characteristic length parameters related to the fracture strength and the fracture toughness.[26]

For propagation in a single crack mode, element refinement as well as coarsening will be considered. However, for mixed-mode crack propagation mode, the approach outlined above will be adopted for refinement only, and coarsening will not be considered in the examples.

6.1 | Double cantilever beam test

The peel test of a double cantilever beam has been chosen as a first illustration of the adaptive hierarchical refinement, see Figure 10. Upon an increase of the external force F, the interface Γ_c will debond progressively. The dimensions of the beam are $l = 10$ mm and $h = 1$ mm. Along the interface, there is an initial traction-free segment with length $b = 1$ mm. The bulk material is modelled as linear isotropic with a Young's modulus $E = 100$ MPa and a Poisson's ratio $\nu = 0.3$. Plane-strain conditions are assumed. The tensile strength and fracture energy are given as $t_u = 1$ MPa and $\mathcal{G}_c = 0.1$ N/mm, respectively. To avoid interpenetration, a penalty stiffness $k_p = 1 \times 10^5$ MPa/mm is specified in the normal direction of Γ_c. A displacement control has been adopted to fully trace the load-displacement path with steps of 0.05mm in the first 20 increments, and steps of 0.2mm in the next 20 increments, and 0.5 mm thereafter.

Initially, the beam has been discretised by linear NURBS with a knot vector $\left(\Xi_1^0, \; \Xi_2^0\right) = ([0 \; 0 \; 1 \; 1], [0 \; 0 \; 1 \; 1])$ and control points $(0, 0)$, $(0, 10)$, $(1, 0)$ and $(10, 1)$. The weight factors w have been taken 1 for all control points. Next, the polynomial degree is increased by order elevation to $p, q = 2$, see Equation 8. The interface Γ_c is introduced in the parametric domain by knot insertion, which leads to $\Xi_2^0 = [0 \; 0 \; 0 \; 0.5 \; 0.5 \; 0.5 \; 1 \; 1 \; 1]$. Then the knot vectors Ξ_1^0 and Ξ_2^0 are equally divided into 20×2 and 40×4 elements, respectively, which yields the final initial knot vector $\left(\Xi_1^0, \; \Xi_2^0\right)$ and the control points $\mathbf{P}^0$. A hierarchy of 3 and 4 levels, respectively, has been used to construct the space of the hierarchical basis functions. To construct such a hierarchy, the knot vector $\left(\Xi_1^I, \; \Xi_2^I\right)$ and the control points $\mathbf{P}^I$ at each hierarchy level are defined by successive uniform knot insertions, starting from the initial knot vector $\left(\Xi_1^0, \; \Xi_2^0\right)$ and the control points $\mathbf{P}^0$.

The force-displacement curve is shown in Figure 11. A good agreement is obtained with results in Verhoosel and de Borst. [13] Moreover, results of a similar quality can be obtained by using a coarser initial mesh (20×2 elements) when increasing the number of hierarchy levels. Figure 12 gives contour plots of displacements and stresses for 2 different load levels. The calculation has been performed for an initial mesh of 40×4 elements. The displacement and stress are smooth in either part of the beam due
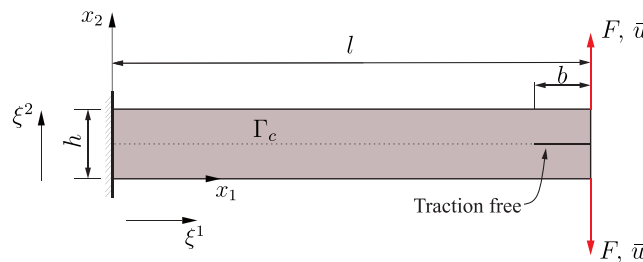
FIGURE 10 Setup of a peel test of a double cantilever beam
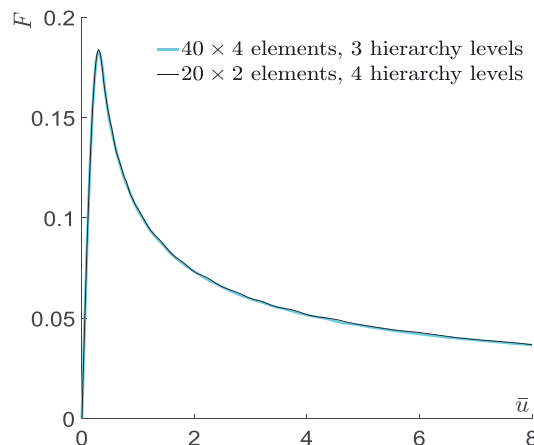
FIGURE 11 Force-displacement curve for the double cantilever beam

(A) u_2 contour plot for $\bar{u} = 0.75$mm   (B) u_2 contour plot for $\bar{u} = 1.0$mm

(C) σ_1 contour plot for $\bar{u} = 0.75$mm   (D) σ_1 contour plot for $\bar{u} = 1.0$mm
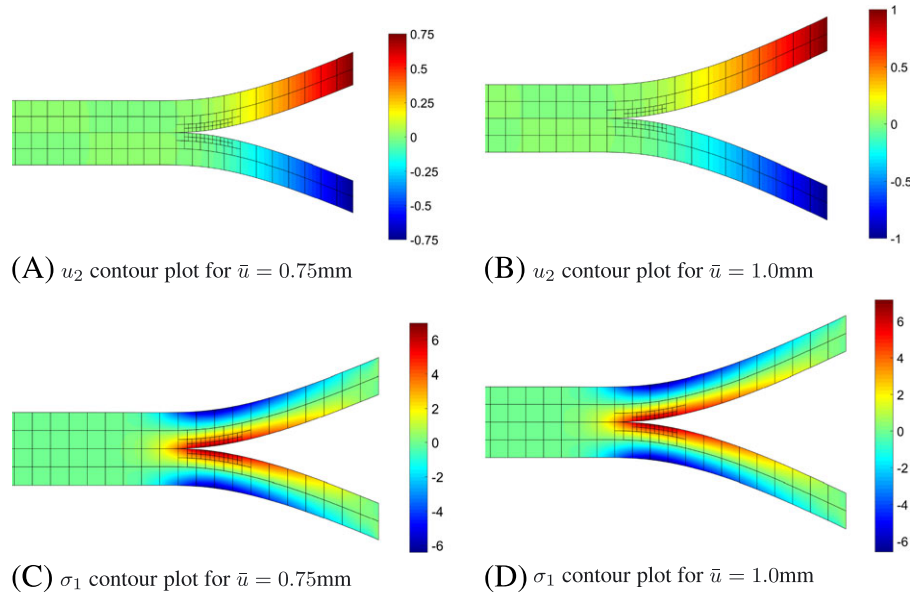
FIGURE 12 Displacements and stress distribution for different load steps (no magnification)
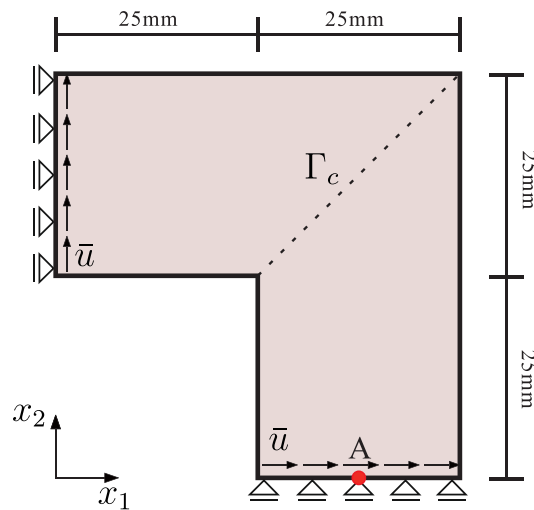
FIGURE 13 L-shaped beam

to the C^1-continuity of the second-order NURBS basis functions. The crack propagates smoothly through the interface Γ_c, and no oscillations in the stresses are observed. Coarsening in the wake of the crack tip has been performed in a manner discussed in Section 4.3.

6.2 | L-shaped beam

Next, the L-shaped beam of Figure 13 is considered. Roller boundary conditions are used, as also shown in the figure. The beam is loaded in the horizontal as well as in the vertical direction by gradually increasing the displacement $\bar{u}$ of the bottom and the left edges. Linear isotropic elasticity is used to describe the bulk material, with a Young's modulus $E = 250$ MPa and a Poisson's ratio $\nu = 0.2$. Plane-strain conditions have been assumed. The interface is indicated by a dashed line along the diagonal of the beam. A Xu-Needleman cohesive zone model has again been used to describe the debonding of the interface with $t_u = 1$ MPa and $\mathcal{G}_c = 0.1$ N/mm. The penetration stiffness is set $k_p = 1 \times 10^5$ MPa/mm to prevent the interpenetration.

At the onset, the beam has been discretised by linear NURBS with the control points $(25, 0)$, $(50, 0)$, $(25, 25)$, $(25, 50)$, $(0, 25)$, $(0, 50)$ and the knot vector $\left(\Xi_1^0, \Xi_2^0\right) = ([0\ 0\ 1\ 1], [0\ 0\ 0.5\ 1\ 1])$. The weight factors w of the control points have been set equal to 1. Next, order elevation is used to increase the polynomial degree to $p, q = 2$, and knot insertion is used to introduce

the interface Γ_c in the parametric domain, which leads to $\Xi_2^0 = [0\ \ 0\ \ 0\ \ 0.5\ \ 0.5\ \ 0.5\ \ 1\ \ 1\ \ 1]$. Eventually, the knot vectors Ξ_2^0 and Ξ_2^0 are divided into 10×20 elements, which generates the final initial knot vector $(\Xi_1^0,\ \Xi_2^0)$ and the control points $\boldsymbol{P}^0$.

A hierarchy of 4 levels is constructed from the initial mesh of 10×20 elements. The response curves for different meshes are presented in Figure 14. A global mesh of 30×60 elements has been used to provide a reference solution. The figure shows that the results obtained using a hierarchy of 4 levels with a coarser initial mesh are in good agreement with the reference solution. Figure 15 shows the radial displacements and the radial stress distribution for a partially propagated crack. The calculation is based on a hierarchy of 4 levels. The stress distribution is again smooth without oscillations around the crack tip. Element refinement and coarsening work smoothly and without problems or need for user intervention.
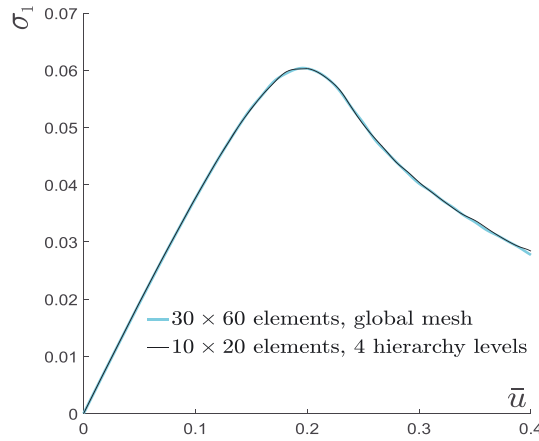
FIGURE 14 Response curves for the L-shaped beam. The stress component σ_1 at $\boldsymbol{x}_A = (37.5,\ \ 0)$ mm is plotted vs the prescribed displacement $\bar{u}$. A global mesh with 30×60 elements is used to provide the reference solution

(A) u_r contour plot under $\bar{u} = 0.2$mm

(B) u_r contour plot under $\bar{u} = 0.4$mm

(C) σ_r contour plot under $\bar{u} = 0.2$mm

(D) σ_r contour plot under $\bar{u} = 0.4$mm
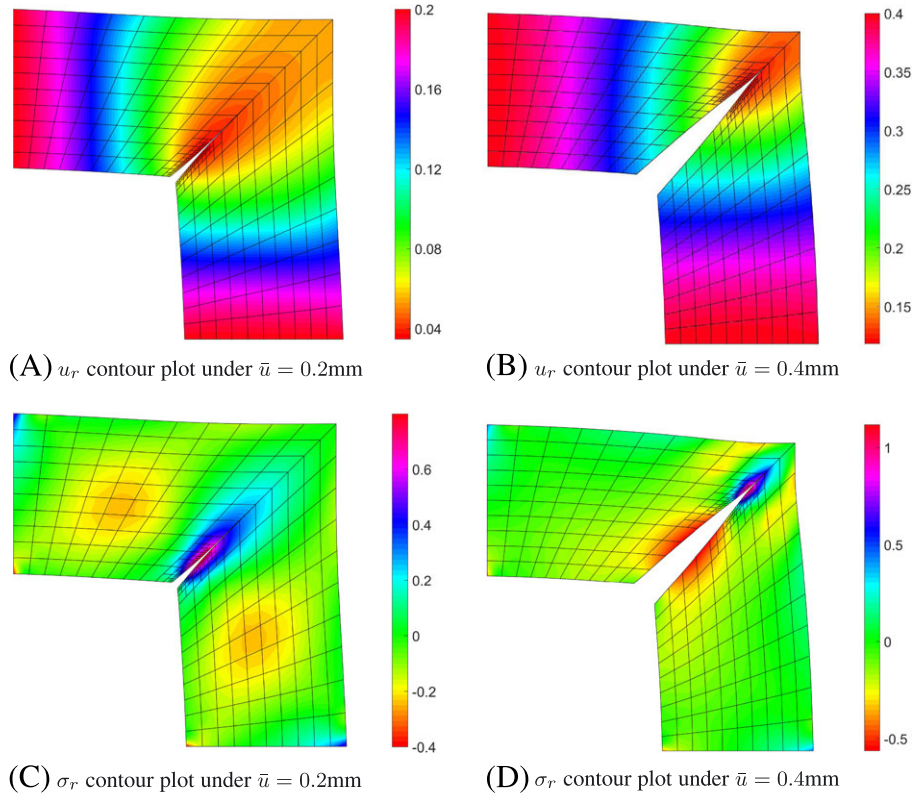
FIGURE 15 Distribution of the radial displacement u_r and the radial stress σ_r in the beam for different load levels. The displacements have been amplified by a factor 10
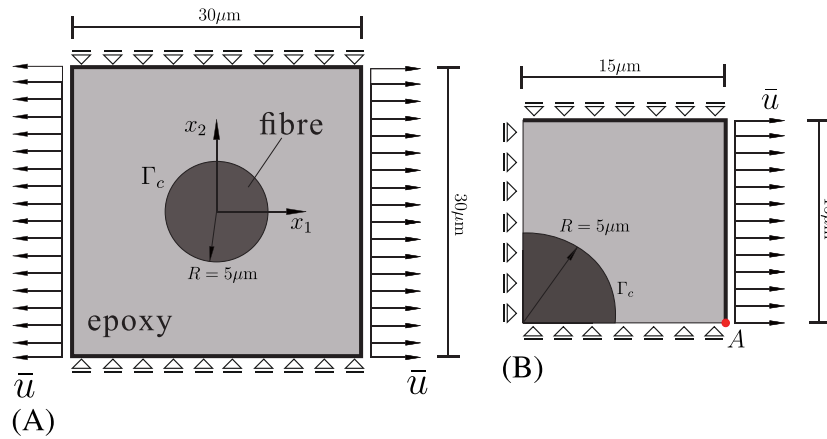
FIGURE 16 Fibre with a circular cross section: problem definition. A, schematic representation of the full model; B, one quarter of the fibre with symmetric boundary conditions
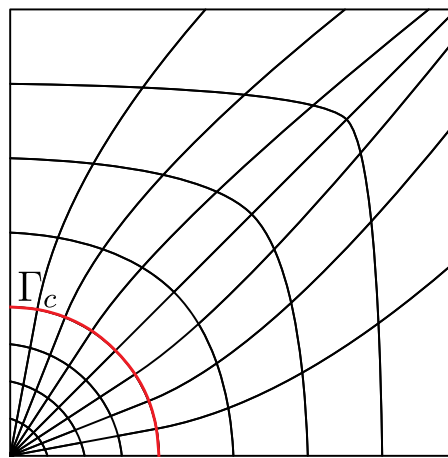
FIGURE 17 Initial mesh for the fibre-epoxy model. The interface Γ_c is indicated by a red circle
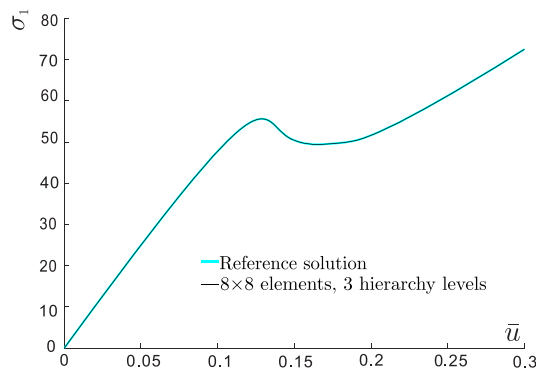
FIGURE 18 Response curves for fibre-epoxy debonding. The stress component σ_1 at $x_A = (15, \quad 0)\,\mu$m is plotted *vs* the prescribed displacement $\bar{u}$

6.3 | Fibre-epoxy debonding

The example of fibre-epoxy debonding has been studied before in Verhoosel et al.[26] The problem is analysed by a two-dimensional model assuming plane-strain conditions. The geometry of the specimen is shown in Figure 16. Because of symmetry, only one quarter of the specimen has been considered with symmetry-enforcing boundary conditions. The material properties are as follows. For the fibre Young's modulus $E = 225\,$GPa and Poisson's ratio $\nu = 0.2$, and for the epoxy, we have a Young's modulus $E = 4.3\,$GPa and a Poisson's ratio $\nu = 0.34$. The tractions at the fibre-epoxy interface have again been assumed

(A) u_1 contour plot under $\bar{u} = 0.1\mu$m   (B) u_1 contour plot under $\bar{u} = 0.2\mu$m

(C) σ_1 contour plot under $\bar{u} = 0.1\mu$m   (D) σ_1 contour plot under $\bar{u} = 0.2\mu$m
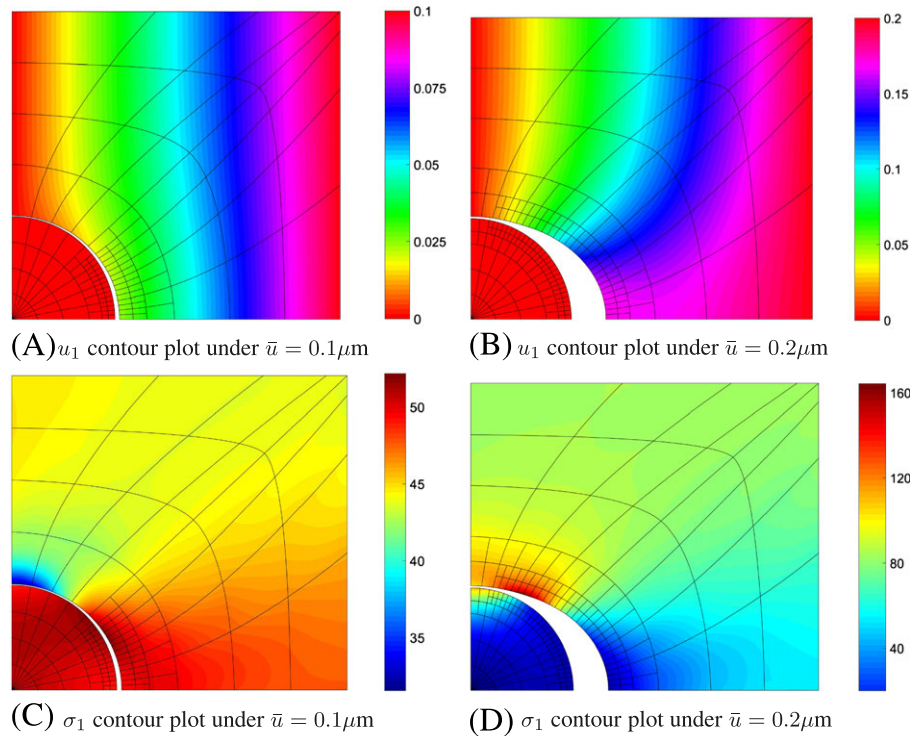
FIGURE 19   Contour plots for the displacements and the stresses at different load levels. The displacements have been amplified by a factor 10

to follow the Xu-Needleman relation with $t_u = 50\,$MPa and $\mathcal{G}_c = 4 \times 10^{-3}$ N/mm. To prevent interpenetration, a penetration stiffness has been added with $k_p = 10^5\,$MPa/mm.

A hierarchy of 3 levels has been constructed on the basis of the initial mesh of Figure 17. The order of the NURBS basis functions is $p, q = 2$. The response curve is presented in terms of the horizontal stress σ_1 as a function of the prescribed displacement $\bar{u}$, see Figure 18. The results agree well with the solution in the literature.[26]

The debonding process of fibre and epoxy is illustrated in Figure 19. The crack propagates gradually with the increase of the prescribed displacement. The element refinement is performed with the crack growth. The stress distribution remains smooth in the fibre and as well as in the epoxy.

7 | CONCLUDING REMARKS

A NURBS basis has been used to represent a crack interface. This has been achieved by knot insertion until C^{-1}-continuity has been attained. To capture the stress state smoothly ahead of the crack tip, hierarchical refinement has been used. A coarse initial mesh was refined by successive knot insertion in the domain of interest. The use of an element-wise point of view to a multilevel mesh allows to dynamically change the mesh during the simulation. Bézier extraction makes it possible to implement the method in any existing finite element code.

Algorithmically, a multilevel mesh is generated by successive knot insertion starting from an initially coarse mesh. Subsequently, the Bézier extraction is applied at each hierarchy level to obtain the stiffness matrix, without considering possible multilevel interactions. This interaction is enforced by a subdivision operator. Two cases have been presented for hierarchical refinement: standard hierarchical refinement and truncated hierarchical refinement. Both algorithms have been elaborated. Moreover, aspects concerning the crack propagation analysis have been illustrated, including the algorithms and implementation aspects for element refinement and coarsening along an interfacial crack.

Numerical examples have been given. They show that the dynamic refinement ability of the hierarchical refinement is suitable for the analysis of crack propagation. The solutions appear to be accurate also for relatively coarse initial meshes. Importantly, the method results in smooth stress fields, which is an appealing aspect for fracture analyses. This holds a fortiori when cracks are considered that do not propagate along predefined interfaces, since the direction of crack propagation is highly influenced by an accurate prediction of the stress field ahead of the crack tip.

ACKNOWLEDGEMENT

REFERENCES

1. Ngo D, Scordelis AC. Finite element analysis of reinforced concrete beams. *J Am Concrete Inst*. 1967;64:152-163.

2. Rashid YR. Analysis of reinforced concrete pressure vessels. *Nucl Eng Des*. 1968;7:334-344.

3. de Borst R. Some recent issues in computational failure mechanics. *Int J Numer Methods Eng*. 2001;52:63-95.

4. de Borst R, Remmers JJC, Needleman A, Abellan MA. Discrete vs smeared crack models for concrete fracture: bridging the gap. *Int J Numer Anal Meth Geomech*. 2004;28:583-607.

5. de Borst R, Gutiérrez MA. A unified framework for concrete damage and fracture models including size effects. *Int J Fract*. 1999;95:261-277.

6. Francfort GA, Marigo JJ. Revisiting brittle fracture as an energy minimization problem. *J Mech Phys Solids*. 1998;46:1319-1342.

7. Bourdin B, Francfort GA, Marigo JJ. The variational approach to fracture. *J Elast*. 2008;91:5-148.

8. Miehe C, Hofacker M, Welschinger F. A phase field model for rate-independent crack propagation: robust algorithmic implementation based on operator splits. *Comput Meth Appl Mech Eng*. 2010;199:2765-2778.

9. Miehe C, Welschinger F, Hofacker M. Thermodynamically consistent phase-field models of fracture: variational principles and multi-field FE implementations. *Int J Numer Meth Eng*. 2010;83:1273-1311.

10. de Borst R, Verhoosel CV. Gradient damage vs phase-field approaches for fracture: similarities and differences. *Comput Meth Appl Mech Eng*. 2016;312:78-94.

11. Bourdin B, Francfort GA, Marigo JJ. Numerical experiments in revisited brittle fracture. *J Mech Phys Solids*. 2000;48:797-826.

12. Borden MJ, Verhoosel CV, Scott MA, Hughes TJR, Landis CM. A phase-field description of dynamic brittle fracture. *Comput Meth Appl Mech Eng*. 2012;217-220:77-95.

13. Verhoosel CV, de Borst R. A phase-field model for cohesive fracture. *Int J Numer Meth Eng*. 2013;96:43-62.

14. Vignollet J, May S, de Borst R, Verhoosel CV. Phase-field models for brittle and cohesive fracture. *Meccanica*. 2014;49:2587-2601.

15. May S, Vignollet J, de Borst R. A numerical assessment of phase-field models for brittle and cohesive fracture: γ-convergence and stress oscillations. *Eur J Mech A/Solids*. 2015;52:72-84.

16. Ingraffea AR, Saouma V. Numerical modelling of discrete crack propagation in reinforced and plain concrete. *Fracture Mechanics of Concrete*. Dordrecht: Martinus Nijhoff Publishers; 1985:171-225.

17. Camacho GT, Ortiz M. Computational modelling of impact damage in brittle materials. *Int J Solids Struct*. 1996;33:2899-2938.

18. Schrefler BA, Secchi S, Simoni L. On adaptive refinement techniques in multifield problems including cohesive fracture. *Comput Meth Appl Mech Eng*. 2006;195:444-461.

19. Secchi S, Simoni L, Schrefler BA. Mesh adaptation and transfer schemes for discrete fracture propagation in porous materials. *Int J Numer Anal Meth Geomech*. 2007;31:331-345.

20. Belytschko T, Black T. Elastic crack growth in finite elements with minimal remeshing. *Int J Numer Meth Eng*. 1999;45:601-620.

21. Moës N, Dolbow J, Belytschko T. A finite element method for crack growth without remeshing. *Int J Numer Meth Eng*. 1999;46:131-150.

22. Fries TP, Belytschko T. The extended/generalized finite element method: an overview of the method and its applications. *Int J Numer Meth Eng*. 2010;84:253-304.

23. Wells GN, Sluys LJ. A new method for modelling cohesive cracks using finite elements. *Int J Numer Meth Eng*. 2001;50:2667-2682.

24. Wells GN, de Borst R, Sluys LJ. A consistent geometrically non-linear approach for delamination. *Int J Numer Meth Eng*. 2002;54:1333-1355.

25. Remmers JJC, de Borst R, Needleman A. A cohesive segments method for the simulation of crack growth. *Comput Mech*. 2003;31:69-77.

26. Verhoosel CV, Scott MA, de Borst R, Hughes TJR. An isogeometric approach to cohesive zone modeling. *Int J Numer Meth Eng*. 2011;87:336-360.

27. Irzal F, Remmers JJC, Verhoosel CV, de Borst R. An isogeometric analysis Bézier interface element for mechanical and poromechanical fracture problems. *Int J Numer Meth Eng*. 2014;97:608-628.

28. Vignollet J, May S, de Borst R. On the numerical integration of isogeometric interface elements. *Int J Numer Meth Eng*. 2015;102:1773-1749.

29. Vignollet J, May S, de Borst R. Isogeometric analysis of fluid-saturated porous media including flow in the cracks. *Int J Numer Meth Eng*. 2016;108:990-1006.

30. May S, de Borst R, Vignollet J. Powell-Sabin B-splines for smeared and discrete approaches to fracture in quasi-brittle materials. *Comput Meth Appl Mech Eng*. 2016;307:193-214.

31. Dimitri R, De Lorenzis L, Wriggers P, Zavarise G. NURBS and T-spline-based isogeometric cohesive zone modeling of interface debonding. *Comput Mech*. 2014;54:369-388.

32. Borden MJ, Scott MA, Evans JA, Hughes TJR. Isogeometric finite element data structures based on Bézier extraction of NURBS. *Int J Numer Meth Eng*. 2011;87:15-47.

33. Scott MA, Borden MJ, Verhoosel CV, Sederberg TW, Hughes TJR. Isogeometric finite element data structures based on Bézier extraction of T-splines. *Int J Numer Meth Eng*. 2011;88:126-156.

34. D. S. Dugdale DS. Yielding of steel sheets containing slits. *J Mech Phys Solids*. 1960;8:100-104.

35. Barenblatt GI. The mathematical theory of equilibrium cracks in brittle fracture. *Adv Appl Mech*. 1962;7:55-129.

36. Xu XP, Needleman A. Void nucleation by inclusion debonding in a crystal matrix. *Modell Simul Mater Sci Eng*. 1993;1:111-132.

37. Remmers JJC, de Borst R, Needleman A. The simulation of dynamic crack propagation using the cohesive segments method. *J Mech Phys Solids*. 2008;56:70-92.

38. Schellekens JCJ, de Borst R. On the numerical integration of interface elements. *Int J Numer Meth Eng*. 1993;36:43-66.

39. de Borst R. Numerical aspects of cohesive-zone models. *Eng Fract Mech*. 2003;70:1743-1757.

40. Schellekens JCJ, de Borst R. Free edge delamination in carbon-epoxy laminates: a novel numerical/experimental approach. *Compos Struct*. 1994;28:357-373.

41. de Borst R, Remmers JJC. Computational modelling of delamination. *Compos Sci Technol*. 2006;66:713-722.

42. Allix O, Ladevèze P. Interlaminar interface modelling for the prediction of delamination. *Compos Struct*. 1992;22:235-242.

43. Allix O, Corigliano A. Geometrical and interfacial non-linerarities in the analysis of delamination in composites. *Int J Solids Struct*. 1999;36:2189-2216.

44. Balzani C, Wagner W. An interface element for the simulation of delamination in unidirectional fiber-reinforced composite laminates. *Eng Fract Mech*. 2008;75:2597-2615.

45. Zander N, Ruess M, Bog T, Kollmannsberger S, Rank E. Multi-level hp-adaptivity for cohesive fracture modelling. *Int J Numer Meth Eng*. 2017;109:1723-1755.

46. Chen L, Dornisch W, Klinkel S. Hybrid collocation-galerkin approach for the analysis of surface represented 3D-solids employing SB-FEM. *Comput Meth Appl Mech Eng*. 2015;295:268-289.

47. Hughes TJR, Cottrell JA, Bazilevs Y. Isogeometric analysis: CAD, finite elements, NURBS, exact geometry and mesh refinement. *Comput Meth Appl Mech Eng*. 2005;194:4135-4195.

48. Fischer P, Klassen M, Mergheim J, Steinmann P, Müller R. Isogeometric analysis of 2D gradient elasticity. *Comput Mech*. 2011;47:325-334.

49. Verhoosel CV, Scott MA, Hughes TJR, de Borst R. An isogeometric analysis approach to gradient damage models. *Int J Numer Meth Eng*. 2011;86:115-134.

50. Kiendl J, Bletzinger KU, Linhard J, Wüchner R. Isogeometric shell analysis with Kirchhoff-Love elements. *Comput Meth Appl Mech Eng*. 2009;198:3902-3914.

51. May S, Vignollet J, de Borst R. Powell-Sabin B-splines and unstructured standard T-splines for the solution of Kichhoff-Love plate theory using Bézier extraction. *Int J Numer Meth Eng*. 2016;107:205-233.

52. Gomez H, Calo VM, Bazilevs Y, Hughes TJR. Isogeometric analysis of the Cahn-Hilliard phase-field model. *Comput Meth Appl Mech Eng*. 2008;197:4333-4352.

53. Kästner M, Metsch P, de Borst R. Isogeometric analysis of the Cahn—Hilliard equation—a convergence study. *J Comput Phys*. 2016;305:360-371.

54. Chen L, Simeon B, Klinkel S. A NURBS based Galerkin approach for the analysis of solids in boundary representation. *Comput Meth Appl Mech Eng*. 2016;305:777-805.

55. Forsey DR, Bartels RH. Hierarchical B-spline refinement. *ACM Siggraph Comput Graphics*. 1988;22:205-212.

56. Kraft R. Adaptive and linearly independent multilevel b-splines. In: Méhauté AL, Rabut C., Schumaker LL, eds. *Surface fitting and multiresolution methods*. Nashville, TN: Vanderbilt University Press; 1997:209-216.

57. Stam J. Exact evaluation of Catmull-Clark subdivision surfaces at arbitrary parameter values. *Proceedings of the 25th Annual Conference on Computer Graphics and Interactive Techniques*. Orlando, FL: ACM; 1998:395-404.

58. Höllig K, Reif U, Wipper J. Weighted extended B-spline approximation of Dirichlet problems. *SIAM J Numer Anal*. 2001;39:442-462.

59. Stam J. On subdivision schemes generalizing uniform B-spline surfaces of arbitrary degree. *Comput Aided Geom Des*. 2001;18:383-396.

60. Vuong AV, Giannelli C, Jüttler B, Simeon B. A hierarchical approach to adaptive local refinement in isogeometric analysis. *Comput Meth Appl Mech Eng*. 2011;200:3554-3567.

61. Schillinger D, Dede L, Scott MA, Evans JA, Borden MJ, Rank E, Hughes TJR. An isogeometric design-through-analysis methodology based on adaptive hierarchical refinement of nurbs, immersed boundary methods, and T-spline CAD surfaces. *Comput Meth Appl Mech Eng*. 2012;249:116-150.

62. Bornemann PB, Cirak F. A subdivision-based implementation of the hierarchical B-spline finite element method. *Comput Meth Appl Mech Eng*. 2013;253:584-598.

63. Scott MA, Thomas DC, Evans EJ. Isogeometric spline forests. *Comput Meth Appl Mech Eng*. 2014;269:222-264.

64. Kuru G, Verhoosel CV, van der Zee KG, van Brummelen EH. Goal-adaptive isogeometric analysis with hierarchical splines. *Comput Meth Appl Mech Eng*. 2014;270:270-292.

65. Verhoosel CV, Van Zwieten GJ, Van Rietbergen B, De Borst R. Image-based goal-oriented adaptive isogeometric analysis with application to the micro-mechanical modeling of trabecular bone. *Comput Meth Appl Mech Eng*. 2015;284:138-164.

66. Evans EJ, Scott MA, Li X, Thomas DC. Hierarchical T-splines: analysis-suitability, Bézier extraction, and application as an adaptive basis for isogeometric analysis. *Comput Meth Appl Mech Eng*. 2015;284:1-20.

67. Jiang W, Dolbow JE. Adaptive refinement of hierarchical B-spline finite elements with an efficient data transfer algorithm. *Int J Numer Meth Eng*. 2015;102:233-256.

68. Hennig P, Müller S, Kästner M. Bézier extraction and adaptive refinement of truncated hierarchical NURBS. *Comput Meth Appl Mech Eng*. 2016;305:316-339.

69. Giannelli C, JüTtler B, Speleers H. THB-splines: the truncated basis for hierarchical splines. *Comput Aided Geom Des*. 2012;29:485-498.

70. Giannelli C, Jüttler B, Speleers H. Strongly stable bases for adaptively refined multilevel spline spaces. *Adv Comput Math*. 2014;40:459-490.

71. Johannessen KA, Remonato F, Kvamsdal T. On the similarities and differences between Classical Hierarchical, Truncated Hierarchical and LR B-splines. *Comput Meth Appl Mech Eng*. 2015;291:64-101.

72. Buffa A, Giannelli C. Adaptive isogeometric methods with hierarchical splines: error estimator and convergence. *Math Models Meth Appl Sci*. 2016;26:1-25.

73. Scott M, Li X, Sederberg TW, Hughes TJR. Local refinement of analysis-suitable T-splines. *Comput Meth Appl Mech Eng*. 2012;213:206-222.

74. Bandara K, Rüberg T, Cirak F. Shape optimisation with multiresolution subdivision surfaces and immersed finite elements. *Comput Meth Appl Mech Eng*. 2016;300:510-539.